12-2008

Computational Analysis of Input-Shaping Control of Microelectromechanical Mirrors

Thomas Starling
Clemson University, tstarling2@gmail.com

Recommended Citation

Starling, Thomas, "Computational Analysis of Input-Shaping Control of Microelectromechanical Mirrors" (2008). *All Theses*. 505.
https://tigerprints.clemson.edu/all_theses/505

COMPUTATIONAL ANALYSIS OF INPUT-SHAPING CONTROL OF MICROELECTROMECHANICAL MIRRORS

A Thesis
Presented to
the Graduate School of
Clemson University

In Partial Fulfillment
of the Requirements for the Degree
Masters of Science
Mechanical Engineering

---

by
Thomas M Starling II
August 2008

Accepted by:
Dr. Gang Li, Committee Chair
Dr. Mohammed Daqaq
Dr. Lonny Thompson

Abstract

Advances in micromachining technology have enabled the design and development of high performance microelectromechanical systems (MEMS). There is a pressing need for control techniques that can be used to improve the dynamic behavior of MEMS such as the response speed and precision. In MEMS applications, open-loop control is attractive as it computes a priori the required system input to achieve desired dynamic behavior without using feedback, thus eliminating the problems associated with closed-loop MEMS control. While the input-shaping control is attractive due to its simplicity, the effectiveness of this control approach depends on the accuracy of the model that is used to compute the input voltage. Accurate modeling of MEMS dynamics is critical in the input-shaping process. Input-shaping MEMS control algorithms based on analytical lumped models have been proposed. It has been shown that step-shaped input voltages can be used to control the structural vibration of MEMS. However, several questions remain to be answered: (1) What are the effects of the higher vibrational modes on the input-shaping control of MEMS? (2) Can the input-shaping technique be improved to control these effects?

In this work, a full 3-D computational code is developed for coupled electromechanical simulation and analysis of electrostatically actuated MEMS. The effect of higher vibrational modes on the input-shaping control of electrostatic micromirros is investigated. We show that, depending on the design of the micromirros, the bending mode of the micromirror structures can have significant effect on the dynamic behavior of the system, which is difficult to suppress by using the step-voltage open-loop control. We employ a numerical optimization procedure to shape the input voltage from the real time dynamic response of the mirror structures. The optimization procedure results in a periodic nonlinear input voltage design that can effectively suppress the bending mode effect.

To Mom

Acknowledgments

I would like to thank my advisor Prof. G. Li for all of his guidance and support during my stay at Clemson. He taught me many things over the last two years, and never stopped watching out for me. This thesis would not have been possible without his expertise and instruction.

I would like to thank the professors who challenged me during my classes at Clemson: Prof. Li, Prof. Jalili, Prof. Joseph, and Prof Law. I would also like to thank Prof. Summers for the experiences in his design class, and for offering help when my last summer didn't go as planned. I also thank Prof Daqaq and Prof Thompson for agreeing to be my thesis committee members.

I would also like to thank the ME staff for all of their help. Without the help of Lindsay, Gwenn, and Tameka I would have been lost.

I would like to thank the FMU Physics and Mathematics Faculty for all of their encouragement during my undergraduate studies. I would especially like to thank Prof Seth Smith for challenging me to be a better student and encouraging me to apply for graduate school.

I would like to acknoledge my family for all of their support and encouragement. My parents have given me invaluable guidance throughout my entire education. I would like to thank my grandfather for his spiritual advice and example. Also, a special thanks to the Childers family for adopting me for the last two years. Mrs. Childers' cooking was second to none and often the only opportunity for me to eat something other than fast food.

Table of Contents

List of Tables

List of Figures

Chapter 1

Introduction

Microelectromechanical systems (MEMS) were first developed in the 1970-80's for use in integrated circuits (IC's)[1]. Since then MEMS have found many applications in optics, communications, microscopes, bio technology, robotics, transportation, and aerospace[2, 3]. Some of the commercialized MEMS include, automotive accelerometers and gyroscopes, pressure sensors, ink-jet print heads, optical RF switching networks, data storage, and disposable chemical analysis systems [4]. Within the large family of MEMS, electrostatically actuated micromirrors have been developed for several applications such as optical RF switches, microscanners and video projectors [5]. Viereck et. al [6] set arrays of mirrors between the two planes of glass in a window to direct sunlight into a room. The mirrors can be operated in a way similar to blinds, but are not as noticeable. Other examples include volumetric displays, biochips used to pattern custom DNA chips, holography, data storage, spectroscopy and ion trap based quantum computing[7, 8]. As the potential applications of mircomirrors are very broad and promising, there is a pressing need for control techniques that can be used to improve the dynamic behavior, such as the response speed and precision, of micromirrors.

Broadly defined, there are two major control approaches available for MEMS control: closed-loop control and open-loop control. From a controls point of view, closed-loop control is preferred as the closed-loop control uses feedback to monitor the state of the system. The closed-loop control is more robust and resistant to fabrication uncertainties, design imperfections and environment disturbances. Therefore, a closed-loop control can guarantee the designed performance. However, in MEMS applications, closed-loop control has significant disadvantages [9]: (1) unlike macro mechanical systems, the implementation of the feedback mechanism is difficult in MEMS due to the small size of the system and the high speed, high frequency operation, (2) the closed-loop control system needs to be integrated on the MEMS system, which could significantly increase the size and the cost of the system, (3) the added control system and circuits can significantly increase the complexity and reduce the reliability of the microdevice. In contrast, open-loop control computes the required system input to achieve desired behavior without using feedback, thus eliminating the potential problems associated with the closed-loop control. For this reason, open-loop control of MEMS has attracted much research interest in the past decade.

Input-shaping control is an open-loop control approach in which a sequence of input impulses are applied in order to generate the desired results [10]. Singer and Singhose are arguably responsible for some of the earlier input shaping techniques [11, 12]. Singhose et. al [13] proposed four input-shaping methods for gantry crane operations: ZV (Zero Vibration), NZV (Negative Zero Vibration), ZVD (Zero Vibration Derivative), and NZVD (Negative Zero Vibration Derivative). In MEMS applications, Borovic et. al. compares open loop control to closed loop control for MEMS in [9] and more specifically a MEMS electrostatic comb drive in [14]. Popa [15] demonstrates the use of input shaping on thermal bimorph MEMS. Yang [16] uses input shaping to suppress the vibration of a cantilever beam. For electrostatic micromirror systems, an input-shaping control algorithm based on analytical lumped models has also been proposed [10]. While the input-shaping control is attractive due to its simplicity, the effectiveness of this control approach depends on the accuracy of the model that is used to compute the input signal. Accurate modeling of MEMS dynamics is critical in the input-shaping process. The above mentioned input-shaping control algorithms are all based on analytical and semi-analytical models with many simplifications of the system. As many MEMS devices have complex geometries and nonlinear behaviour, it is not clear to what extend these models are accurate. In addition, it is not clear what the effects of the higher vibrational modes are on the input-shaping control of MEMS and if it is possible to improve the input-shaping technique to control these effects.

To address these issues, accurate modeling of MEMS dynamics is required. Based on the level of abstraction, MEMS modeling approaches can be categorized into three groups: analytical/semi-analytical approach, reduced order approach and full numerical approach. In the analytical/semi-analytical approach, the MEMS device is discretized into a mass, spring, damper system or by using more complex methods involving vibrations of continuous media [10,17,18]. This approach requires a certain familiarity with MEMS physics. Two difficulties associated with this approach are (1) not having a standard method for producing these macromodels, and (2) the lack of methods for verification of the macromodels' accuracy [18]. The reduced order modeling approach can be further divided into numerical order reduction approaches and circuit-based approaches. In the numerical model reduction approach, the system equations are solved approximately in order to reduce the order of the system [18, 19]. However, if the system has nonlinearities it becomes difficult to perform nonlinear model reduction. This method is not accurate enough for use in both control optimization and design synthesis. The circuit-based approaches breaks the MEMS device into a circuit composed of anchors, beams, gaps, and plates. This approach allows for verification, but some designs cannot be supported by this method. The third approach is the full numerical approach that discretize the system directly and solves the governing partial differential equations directly [20,21]. The full numerical approach is general and accurate compared to other approaches. Since an accurate model is important in MEMS open-loop controls, in this work, we adopt the full numerical approach to investigate electrostatic micromirrors.

The numerical analysis of MEMS typically involves a mechanical analysis and an electrostatic analysis. In this thesis, the Finite Element Method (FEM) is utilized in mechanical analysis because of its accuracy and robustness. The Boundary Element Method is utilized to solve the boundary integral equations (BIE) of the electrostatics problem. The BEM offers an accurate solution to the electrostatic forces, which are often approximated by means of analytical methods. We have developed a full 3-D general purpose FEM/BEM solver for coupled electromechanical simulation and analysis of electrostatically actuated MEMS. On top of the FEM/BEM solver, input-shaping open-loop control algorithms are also implemented. The effect of higher vibrational modes on the input-shaping control of electrostatic micromirros is investigated. We show that, depending on the design of the micromirros, the bending mode of the micromirror structures can have significant effect on the dynamic behavior of the system, which is difficult to suppress by using the step-voltage open-loop control. We employ a numerical optimization procedure to shape the input voltage from the real time dynamic response of the mirror structures. The optimization procedure results in a periodic nonlinear input voltage design that can effectively suppress the bending mode effect. The coupled solver presented in this thesis can be used for a number of purposes. The functionalities of the solver include: elastostatic analysis, modal analysis, elastodynamic analysis, electrostatic analysis, static coupled electromechanical analysis, dynamic coupled electromechanical analysis and input-shaping open-loop control analysis.

In our input-shaping open-loop control analysis, we consider the micromirror device shown in Figure 1.1. The mirror consists of two identical microbeams of length l, width w, and thickness h. The beams are fixed on one side and connected to a rigid rectangular plate (the mirror) on the other side. The mirror has a length L_m, width a and thickness h. Beneath the micromirror are two electrodes, each of length L_m and width $(a_2 - a_1)/2$. The gap between the undeformed position of the mirror and the electrodes is denoted as d. The whole microstucture is etched out of a silicon substrate that has a density ρ, a Young's Modulus E, and a Poisson's ratio of ν. We investigate the dynamic response of three different designs of the micromirror. In all three design, the size of the mirror plate and the electrodes are the same. In the first design (Mirror A), the length of the suspension beams is relatively short and the electrodes are positioned align with the outer edges of the mirror plate. The second design (Mirror B) has the same design parameters as those in Mirror A except that the electrodes are placed more towards the center of the mirror plate. In the third design, the beam length is increased and the electrodes are placed close the center of the mirror plate. The material properties and dimensions of the mirrors are listed in Table 1.1.

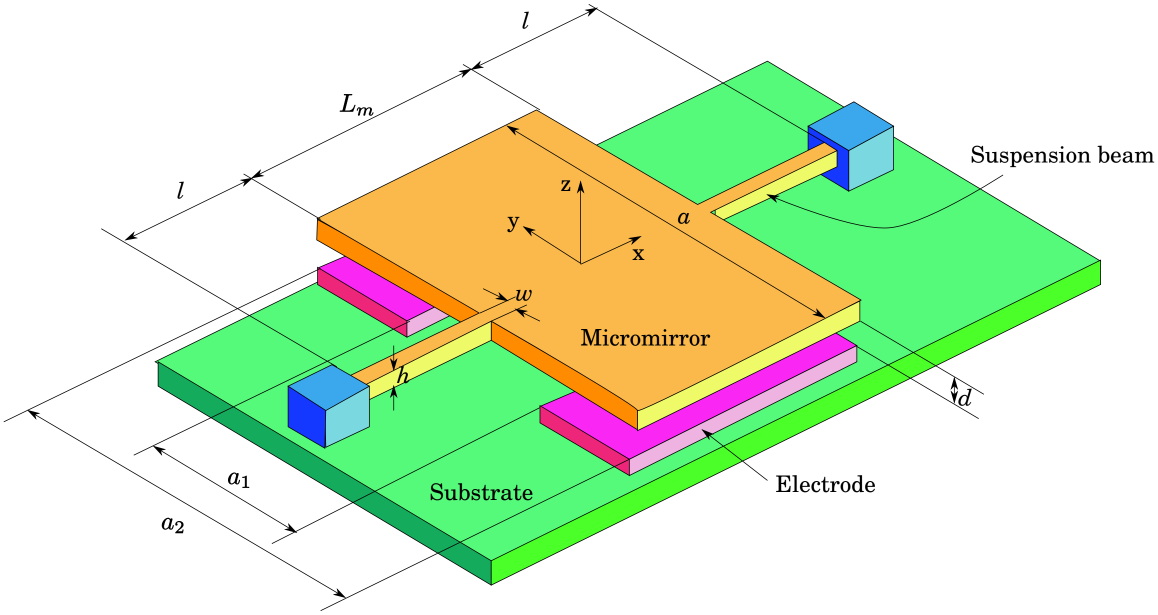

Figure 1.1: Schematic diagram of the torsional micromirror

The mirror is activated to rotate in either direction by supplying a voltage $V(t)$ to

Table 1.1: Material properties and dimensions of the torsional micromirrors.

Properties			
Modulus of elasticity, E (GPa)	170		
Poisson's ratio	0.3		
Density, ρ (kg/m^3)	2330		
Dielectric contant of air, ϵ_0 (F/m)	$8.85{\times}10^{-12}$		
Dimensions	Mirror A	Mirror B	Mirror C
Mirror width, a (μm)	100	100	100
Mirror length, L_m (μm)	100	100	100
Beam length, l (μm)	45	45	65
Beam width, w (μm)	1.55	1.55	2
Beam thickness, h (μm)	1.50	1.50	1.50
Electrode length, b (μm)	100	100	100
Electrode parameter, $\alpha = \frac{a_1}{a}$	0.3	0.18	0.06
Electrode parameter, $\beta = \frac{a_2}{a}$	1.0	0.78	0.78
Gap height, d (μm)	2.75	2.75	2.75

the corresponding electrode. This results in an electrostatic potential between the electrode and the mirror, which generates electric charges on the lower surface of the mirror and the top surface of the electrode, and hence produces a downward electrostatic force to the mirror plate and an electrostatic moment around the suspension point. Consequently, the microbeams undergo simultaneous rotation and deflection. When the mirror deforms, the electric field between the mirror plate and the electrodes changes and the electric charge redistributes causing a change in electrostatic force. Therefore, an iterative procedure is required to obtain an consistent solution between the mechanical and electrostatic domains.

The rest of the thesis is organized as follows: In Chapter 2, we present the theory and implementation of the Finite Element Method for mechanical analysis. The theory and implementation of the Boundary Element Method are discussed in Chapter 3. The coupling of the FEM and BEM for the coupled electromechanical analysis of MEMS is discuss in Chapter 4. Chapter 5 discusses the input-shaping open-loop control analysis of the micromirrors. Conclusions are given in Chapter 6.

Chapter 2

Finite Element Dynamic Structural Analysis

2.1 Mathematical Model

As shown in Figure 1.1, when a voltage is applied to the electrodes an electrostatic force will act on the mirror in the form of a surface traction, the microbeams and the mirror plate undergo simultaneous rotation and deflection. Since the rotation and deflection are in different planes, a full 3-D simulation is necessary. The gap between the mirror plate and the electrodes is small as shown in Table 1.1. Due to the pull-in effect, the actual rotation of the mirror is even smaller compared to the dimension of the mirror structure. Typically the rotation angle is about 1^o. Therefore, a linear elasticity theory can be used for the mechanical analysis.

The derivation of the discretized dynamic equations of motion in the finite element mechanical analysis is summarized in this section. The method presented hereafter is standard and can be found in FEA textbooks [22,23,24]. To obtain the equations of motion for 3D FEA the mirror structure is discretized into elements. The displacement for each element can then be written as

$$\mathbf{u}^{(e)}(x,y,z,t) = \left\{ \begin{array}{c} u(x,y,z,t) \\ \\ v(x,y,z,t) \\ \\ z(x,y,z,t) \end{array} \right\} = \mathbf{N}(x,y,z)\mathbf{d}^{(e)}(t) \tag{2.1}$$

where $\mathbf{u}$ is the displacement vector, $\mathbf{N}(x,y,z)$ are shape functions, $\mathbf{d}$ is the time dependant nodal displacements, and (e) denotes an element. The shape functions are the Lagrange interpolating polynomials that are used to approximate the solution, and are determined by the placement of the nodes in each element. The element strain, $\epsilon^{(e)}$, and stresses, $\sigma^{(e)}$ can then be written as

$$\epsilon^{(e)} = \mathbf{B}\mathbf{d}^{(e)} \tag{2.2}$$

$$\sigma^{(e)} = \mathbf{D}\epsilon^{(e)} \tag{2.3}$$

where $\mathbf{B}$ is the strain-displacement matrix containing first order derivatives of the shape functions [23]. $\mathbf{B}$ can be written as

$$\mathbf{B} = [\mathbf{B}_1\mathbf{B}_2...\mathbf{B}_{n_e}] \tag{2.4}$$

where n_e is the number of nodes in each element and $\mathbf{B}_i$, $i = 1, 2, ..., n_e$, is given by

$$\mathbf{B}_i = \begin{bmatrix} \frac{\partial N_i}{\partial x} & 0 & 0 \\ 0 & \frac{\partial N_i}{\partial y} & 0 \\ 0 & 0 & \frac{\partial N_i}{\partial z} \\ \frac{\partial N_i}{\partial y} & \frac{\partial N_i}{\partial x} & 0 \\ 0 & \frac{\partial N_i}{\partial z} & \frac{\partial N_i}{\partial y} \\ \frac{\partial N_i}{\partial z} & 0 & \frac{\partial N_i}{\partial x} \end{bmatrix} \tag{2.5}$$

$\mathbf{D}$ is the material tensor given by [23]

$$\mathbf{D} = \frac{E}{1-\nu^2} \begin{bmatrix} 1-\nu & \nu & \nu & 0 & 0 & 0 \\ \nu & 1-\nu & \nu & 0 & 0 & 0 \\ \nu & \nu & 1-\nu & 0 & 0 & 0 \\ 0 & 0 & 0 & \frac{1-2\nu}{2} & 0 & 0 \\ 0 & 0 & 0 & 0 & \frac{1-2\nu}{2} & 0 \\ 0 & 0 & 0 & 0 & 0 & \frac{1-2\nu}{2} \end{bmatrix} \tag{2.6}$$

where E is the Young's Modulus of Elasticity and ν is the Poisson's ratio. The velocity is approximated by differentiating (2.1) with respect to time

$$\dot{\mathbf{u}}^{(e)}(x,y,z,t) = \mathbf{N}(x,y,z)\dot{\mathbf{d}}^{(e)}(t) \tag{2.7}$$

where $\dot{\mathbf{d}}^{(e)}(t)$ is the nodal velocity of element (e). The equations of motion can be found by using Lagrange's equations [23,25]

$$\frac{d}{dt}\left(\frac{\partial L}{\partial \dot{\mathbf{u}}}\right) - \frac{\partial L}{\partial \mathbf{u}} + \frac{\partial R}{\partial \dot{\mathbf{u}}} = \mathbf{0} \tag{2.8}$$

where R is the dissipation function or damping,

$$L = T - \pi_p \tag{2.9}$$

is the Lagrangian, T is the kinetic energy, and π_p is the potential energy. The kinetic energy for an element can be expressed as

$$T^{(e)} = \frac{1}{2}\iiint_{V^{(e)}} \rho \dot{\mathbf{u}}^{(e)^T} \dot{\mathbf{u}}^{(e)} dV. \tag{2.10}$$

where ρ is the mass density, and $V^{(e)}$ is element volume. The potential energy, $\pi_p^{(e)}$, for an element can be expressed as

$$\pi_p^{(e)} = \frac{1}{2}\iiint_{V^{(e)}} \epsilon^{(e)^T}\sigma^{(e)} dV - \iint_{\Gamma_h^{(e)}} \mathbf{u}^{(e)^T}\mathbf{h} d\Gamma - \iiint_{V^{(e)}} \mathbf{u}^{(e)}\boldsymbol{\phi} dV. \tag{2.11}$$

where $\Gamma_h^{(e)}$ is the element surface, $\mathbf{h}$ and $\boldsymbol{\phi}$ are the surface traction and the body force, respectively,

$$\mathbf{h} = \left\{ \begin{array}{c} h_x \\ \\ h_y \\ \\ h_z \end{array} \right\} \qquad\qquad \boldsymbol{\phi} = \left\{ \begin{array}{c} \phi_x \\ \\ \phi_y \\ \\ \phi_z \end{array} \right\} \tag{2.12}$$

In Eq. (2.11) the only forces present are surface and body forces, concentrated point loads are not represented in the element potential energy. Concentrated point forces are taken into account in the global potential energy. The element dissipation function $R^{(e)}$ can be written as

$$R^{(e)} = \frac{1}{2} \iiint_{V^{(e)}} \mu \dot{\mathbf{u}}^{(e)^T} \dot{\mathbf{u}}^{(e)} dV \tag{2.13}$$

where μ is the damping coefficient. Equations (2.1) - (2.3) can be substituted into (2.10) - (2.13) to get

$$T = \sum_{e=1}^{N} T^{(e)} = \sum_{e=1}^{N} \left[\frac{1}{2} \dot{\mathbf{d}}^{(e)^T} \left(\iiint_{V^{(e)}} \rho \mathbf{N}^T \mathbf{N} dV \right) \dot{\mathbf{d}}^{(e)} \right] \tag{2.14}$$

$$\begin{aligned} \pi_p = \sum_{e=1}^{N} \pi_p^{(e)} - \mathbf{d}^T \mathbf{p}_c = \sum_{e=1}^{N} \Bigg[& \left(\frac{1}{2} \mathbf{d}^{(e)^T} \iiint_{V^{(e)}} \mathbf{B}^T \mathbf{D} \mathbf{B} dV \right) \mathbf{d}^{(e)} \\ & - \left(\mathbf{d}^{(e)^T} \iint_{\Gamma_h^{(e)}} \mathbf{N}^T \mathbf{h} d\Gamma + \mathbf{d}^{(e)^T} \iiint_{V^{(e)}} \mathbf{N}^T \boldsymbol{\phi} dV \right) \Bigg] - \mathbf{d}^T \mathbf{p}_c \end{aligned} \tag{2.15}$$

$$R = \sum_{e=1}^{N} T^{(e)} = \sum_{e=1}^{N} \left[\frac{1}{2} \dot{\mathbf{d}}^{(e)^T} \iiint_{V^{(e)}} \mu \mathbf{N}^T \mathbf{N} dV \right] \dot{\mathbf{d}}^{(e)} \tag{2.16}$$

where N is the number of elements, $\mathbf{N}$ is a matrix of shape functions, $\mathbf{p}_c$ is the concentrated point loads and $\mathbf{d}$ is the global nodal displacement vector. To simplify the Lagrangian, let

$$\begin{aligned}
\mathbf{M}^{(e)} &= \text{element mass matrix} = \iiint_{V^{(e)}} \rho \mathbf{N}^T \mathbf{N} dV && (2.17) \\
\mathbf{K}^{(e)} &= \text{element stiffness matrix} = \iiint_{V^{(e)}} \mathbf{B}^T \mathbf{D} \mathbf{B} dV && (2.18) \\
\mathbf{C}^{(e)} &= \text{element damping matrix} = \iiint_{V^{(e)}} \mu \mathbf{N}^T \mathbf{N} dV && (2.19) \\
\mathbf{p}_s^{(e)} &= \text{vector of element surface traction} = \iint_{\Gamma_h^{(e)}} \mathbf{N}^T \mathbf{h} d\Gamma && (2.20) \\
\mathbf{p}_b^{(e)} &= \text{vector of element body forces} = \iiint_{V^{(e)}} \mathbf{N}^T \boldsymbol{\phi} dV && (2.21)
\end{aligned}$$

Equations (2.14) - (2.16) can be rewritten as

$$\begin{aligned}
T &= \sum_{e=1}^{N} \left(\frac{1}{2} \dot{\mathbf{d}}^{(e)^T} \mathbf{M}^{(e)} \dot{\mathbf{d}}^{(e)} \right) && (2.22) \\
\pi_p &= \sum_{e=1}^{N} \left[\frac{1}{2} \mathbf{d}^{(e)^T} \mathbf{K}^{(e)} \mathbf{d}^{(e)} - \left(\mathbf{d}^{(e)^T} \mathbf{p}_s^{(e)} + \mathbf{d}^{(e)^T} \mathbf{p}_b^{(e)} \right) \right] - \mathbf{d}^T \mathbf{p}_c && (2.23) \\
R &= \sum_{e=1}^{N} \left[\frac{1}{2} \dot{\mathbf{d}}^{(e)^T} \mathbf{C}^{(e)} \dot{\mathbf{d}}^{(e)} \right] && (2.24)
\end{aligned}$$

T, π_p, and R can now be written in the global form

$$\begin{aligned}
T &= \frac{1}{2} \dot{\mathbf{d}}^T \mathbf{M} \dot{\mathbf{d}} && (2.25) \\
\pi_p &= \frac{1}{2} \mathbf{d}^T \mathbf{K} \mathbf{d} - \mathbf{d}^T \mathbf{p}_s^{(e)} - \mathbf{d}^T \mathbf{p}_b^{(e)} - \mathbf{d}^T \mathbf{p}_c && (2.26) \\
R &= \frac{1}{2} \dot{\mathbf{d}}^T \mathbf{C} \dot{\mathbf{d}} && (2.27)
\end{aligned}$$

where

$$\mathbf{d} = \text{assemble}(\mathbf{d}^{(e)}, e = 1 \dots N) \tag{2.28}$$

$$\mathbf{M} = \text{assemble}(\mathbf{M}^{(e)}, e = 1 \dots N) \tag{2.29}$$

$$\mathbf{K} = \text{assemble}(\mathbf{K}^{(e)}, e = 1 \dots N) \tag{2.30}$$

$$\mathbf{C} = \text{assemble}(\mathbf{C}^{(e)}, e = 1 \dots N) \tag{2.31}$$

$$\mathbf{P} = \text{assemble}\left(\left(\mathbf{p}_s^{(e)} + \mathbf{p}_b^{(e)}\right), e = 1 \dots N\right) + \mathbf{p}_c \tag{2.32}$$

where $\mathbf{M}$, $\mathbf{C}$, $\mathbf{K}$ are the global mass, damping and stiffness matrices, respectively, and the force vector $\mathbf{P}$ is the summation of all the forces on the structure. Applying Lagrange's equations produces the dynamic equations of motion

$$\mathbf{M}\ddot{\mathbf{d}} + \mathbf{C}\dot{\mathbf{d}} + \mathbf{K}\mathbf{d} = \mathbf{P}. \tag{2.33}$$

where $\ddot{\mathbf{d}}$ is the acceleration vector and $\dot{\mathbf{d}}$ is the velocity vectors.

In the static case, the equations of motion can be easily reduced to the equations of equilibrium by simply setting velocity and acceleration equal to zero. The static equation of equilibrium can be written as

$$\mathbf{K}\mathbf{d} = \mathbf{P}. \tag{2.34}$$

2.2 Discretization and approximation

In this work, we perform the discretization of the mirror structure and obtain the mesh by using commercial FEA packages such as ANSYS and ABAQUS. Since most of the deformation will take place on the beams and the corners where the beams connect to the plate are points of stress concentration, a fine mesh is generated for the beams and the beam-plate connection regions. The mirror plate can be accurately approximated with a course mesh. A sample mesh generated in ABAQUS is shown in Figure 2.1. Linear eight node isoparametric brick elements are employed in our mechanical analysis. Figures 2.2 and 2.3 show a hexahedral eight node brick element and the master element, respectively. The nodal coordinates for the brick element in the local coordinate system are listed in Table (2.1). Using the values from Table (2.1) the shape functions for the brick element can be written as [23 , 24]

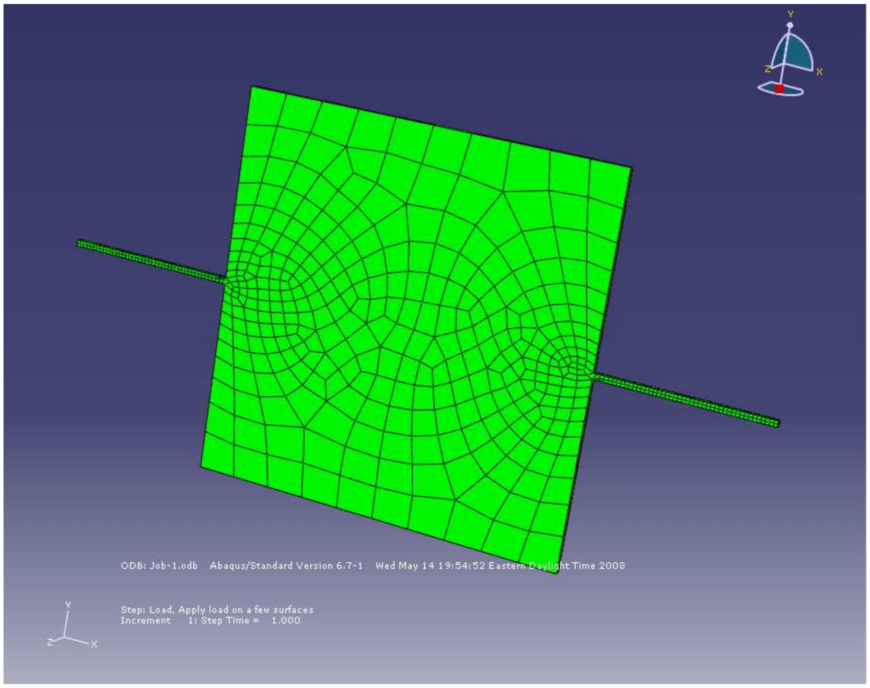

ODB: Job-1.odb Abaqus/Standard Version 6.7-1 Wed May 14 19:54:52 Eastern Daylight Time 2008

Step: Load, Apply load on a few surfaces
Increment 1: Step Time = 1.000

Figure 2.1: Mirror meshing.

$$N_i(\xi, \eta, \zeta) = \frac{1}{8}(1 + \xi_i\xi)(1 + \eta_i\eta)(1 + \zeta_i\zeta) \tag{2.35}$$

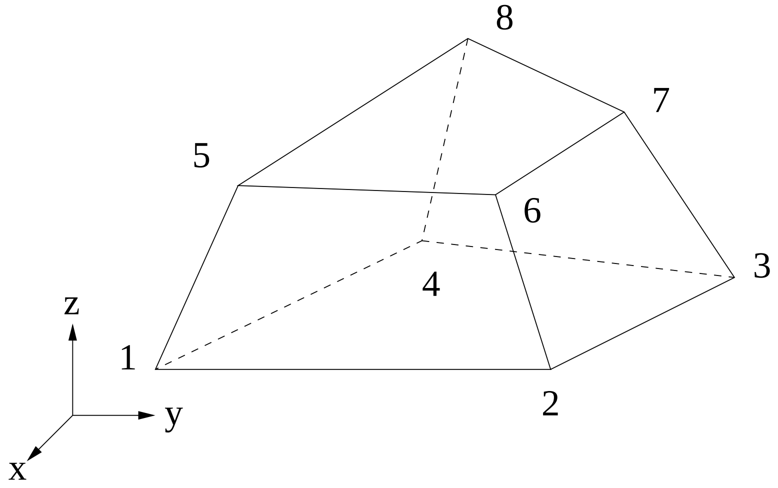

Figure 2.2: Linear hexahedral brick element.

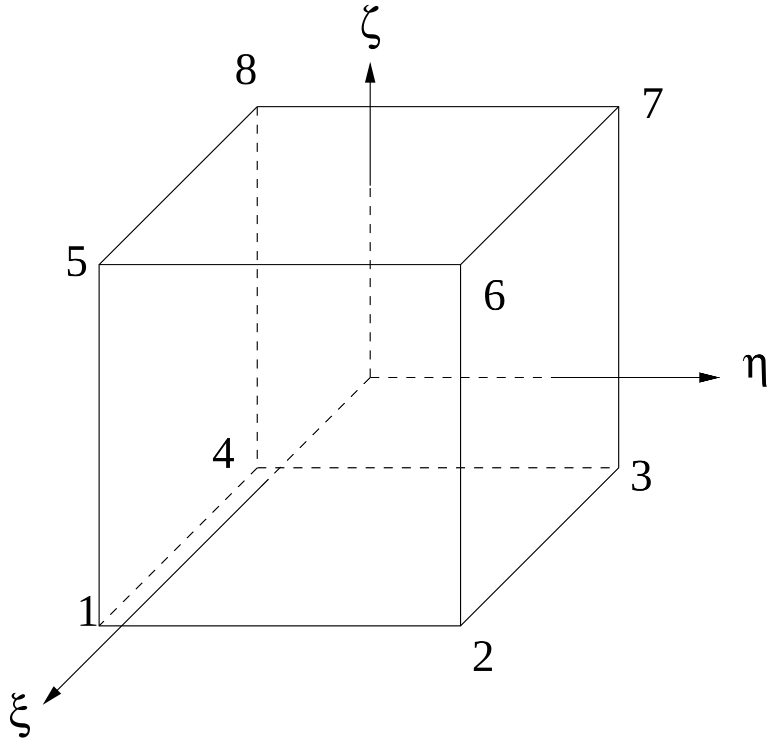

Figure 2.3: 8-node hexahedral master element.

Table 2.1: Nodal coordinates for the brick element in the local coordinate system.

i	ξ_i	η_i	ζ_i
1	-1	-1	-1
2	1	-1	-1
3	1	1	-1
4	-1	1	-1
5	-1	-1	1
6	1	-1	1
7	1	1	1
8	-1	1	1

The derivatives of the shape functions with respect to ξ, η and ζ can be computed by

$$\begin{aligned} \frac{\partial N_i}{\partial \xi} &= \frac{1}{8}\xi_i(1+\eta_i\eta)(1+\zeta_i\zeta) \\ \frac{\partial N_i}{\partial \eta} &= \frac{1}{8}\eta_i(1+\xi_i\xi)(1+\zeta_i\zeta) \\ \frac{\partial N_i}{\partial \zeta} &= \frac{1}{8}\zeta_i(1+\xi_i\xi)(1+\eta_i\eta). \end{aligned} \tag{2.36}$$

The derivatives of the shape functions with respect to x, y and z can be obtained from application of the chain rule:

$$\left\{ \begin{array}{c} \frac{\partial N_i}{\partial \xi} \\ \frac{\partial N_i}{\partial \eta} \\ \frac{\partial N_i}{\partial \zeta} \end{array} \right\} = \mathbf{J} \left\{ \begin{array}{c} \frac{\partial N_i}{\partial x} \\ \frac{\partial N_i}{\partial y} \\ \frac{\partial N_i}{\partial z} \end{array} \right\} \tag{2.37}$$

where $\mathbf{J}$ is the Jacobian. The Jacobian is the scaling factor from the original element to the master element

$$\mathbf{J} = \begin{bmatrix} \sum_{i=1}^{8}\left(\frac{\partial N_i}{\partial \xi}x_i\right) & \sum_{i=1}^{8}\left(\frac{\partial N_i}{\partial \xi}y_i\right) & \sum_{i=1}^{8}\left(\frac{\partial N_i}{\partial \xi}z_i\right) \\ \sum_{i=1}^{8}\left(\frac{\partial N_i}{\partial \eta}x_i\right) & \sum_{i=1}^{8}\left(\frac{\partial N_i}{\partial \eta}y_i\right) & \sum_{i=1}^{8}\left(\frac{\partial N_i}{\partial \eta}z_i\right) \\ \sum_{i=1}^{8}\left(\frac{\partial N_i}{\partial \zeta}x_i\right) & \sum_{i=1}^{8}\left(\frac{\partial N_i}{\partial \zeta}y_i\right) & \sum_{i=1}^{8}\left(\frac{\partial N_i}{\partial \zeta}z_i\right) \end{bmatrix} \tag{2.38}$$

2.3 Integration

The global mass matrix is the assembly of all the element matrices. The element mass, damping and stiffness matrices are given in Eq. (2.17-2.19) as

$$\mathbf{M}^{(e)} = \iiint_{V^{(e)}} \rho \mathbf{N}^T \mathbf{N} dV \tag{2.39}$$

$$\mathbf{C}^{(e)} = \iiint_{V^{(e)}} \mu \mathbf{N}^T \mathbf{N} dV \tag{2.40}$$

$$\mathbf{K}^{(e)} = \iiint_{V^{(e)}} \mathbf{B}^T \mathbf{D} \mathbf{B} dV \tag{2.41}$$

Proportional damping can be used as an alternative to the damping matrix defined in Eq. (2.40). Proportional damping implies that the damping is a proportional function of the mass and stiffness, i.e.,[23]

$$\mathbf{C} = c_1 \mathbf{M} + c_2 \mathbf{K} \tag{2.42}$$

where c_1 and c_2 are mass and stiffness damping constants. The element surface traction and body force vectors are given by

$$\mathbf{p}^{(e)} = \iint_{\Gamma_h} \mathbf{N}^T \mathbf{h} d\Gamma + \iiint_{V^{(e)}} \mathbf{N}^T \boldsymbol{\phi} dV \tag{2.43}$$

The volume and surface integrations for the element matrices and vectors are performed numerically by using Gaussian Quadrature in the local coordinate system. The mass and stiffness element matrices can now be written as

$$\mathbf{K}^{(e)} = \int_{-1}^{1} \int_{-1}^{1} \int_{-1}^{1} \mathbf{B}^T \mathbf{D} \mathbf{B} det(\mathbf{J}) d\xi d\eta d\zeta \tag{2.44}$$

and

$$\mathbf{M}^{(e)} = \int_{-1}^{1} \int_{-1}^{1} \int_{-1}^{1} \rho \mathbf{N}(\xi_g, \eta_g, \zeta_g)^T \mathbf{N}(\xi_g, \eta_g, \zeta_g) det(\mathbf{J}) d\xi d\eta d\zeta \tag{2.45}$$

where $det(\mathbf{J})$ is the determinate of the Jacobian Matrix and ξ_g, η_g, and ζ_g are the coordinates for the g^{th} Gauss Point. Applying the Gaussian quadrature numerical integration, $\mathbf{K}^{(e)}$ and $\mathbf{M}^{(e)}$ can now be rewritten as

$$\mathbf{K}^{(e)} = \sum_{g=1}^{NG} \mathbf{B}^T(\xi_g, \eta_g, \zeta_g) \mathbf{D} \mathbf{B}(\xi_g, \eta_g, \zeta_g) det(\mathbf{J}(\xi_g, \eta_g, \zeta_g)) w_g \tag{2.46}$$

and

$$\mathbf{M}^{(e)} = \sum_{g=1}^{NG} \rho \mathbf{N}(\xi_g, \eta_g, \zeta_g)^T \mathbf{N}(\xi_g, \eta_g, \zeta_g) det(\mathbf{J}(\xi_g, \eta_g, \zeta_g)) w_g \tag{2.47}$$

where NG is the number of Gauss points and w_g is the weight of the g^{th} Gauss point and

$$\mathbf{N}(\xi_g,\eta_g,\zeta_g) = \begin{bmatrix} N_1(\xi_g,\eta_g,\zeta_g) & 0 & 0 \\ 0 & N_1(\xi_g,\eta_g,\zeta_g) & 0 \\ 0 & 0 & N_1(\xi_g,\eta_g,\zeta_g) \\ \vdots & \vdots & \vdots \\ N_8(\xi_g,\eta_g,\zeta_g) & 0 & 0 \\ 0 & N_8(\xi_g,\eta_g,\zeta_g) & 0 \\ 0 & 0 & N_8(\xi_g,\eta_g,\zeta_g) \end{bmatrix} \tag{2.48}$$

where each shape function is evaluated at the g^{th} Gauss point.

For the surface traction case, the surface traction acts on an area instead of a volume, a cross product of two of the columns in the 3D Jacobian matrix will yield the area Jacobian for the surface integration. The method for utilizing this principle can be written as [24]

$$\int_{\Gamma_h} \mathbf{N}\mathbf{h}d\Gamma = \int_{-1}^{1}\int_{-1}^{1} \mathbf{N}\mathbf{h}\|\mathbf{x}_{,\xi} \times \mathbf{x}_{,\eta}\| d\xi d\eta \tag{2.49}$$

After the element matrices and vectors are calculated the global matrices and vectors can be assembled. The assembly for the mass and stiffness matrices are the same, and since the damping matrix is derived from the mass and stiffness matrices there is no assembly required. The first step in assembling the global matrices is determining the node numbers. There are two node numbers, the local element node number and the global node number. The element node number determines where the node belongs with respect to the element. The global node number determines where the node belongs with respect to the model. In addition, the local node number pertains to the node's placement within the element matrix while the global node number pertains to the node's placement within the global matrix. The dimensions of the element matrices are 24x24. This can also be regarded as 8x8 blocks with each block being a 3x3 matrix. Each 3x3 matrix has a corresponding 3x3 block in the global matrix. The direct relationship between the element matrix and the global matrix can be expressed as

$$M(3*(GN\#_i)+k,3*(GN\#_j)+l)=m^{(e)}(3*i+k,3*j+l) \tag{2.50}$$

Where i and j are local node numbers, k and l are the positions in the individual 3x3 matrices, and $GN\#_i$ and $GN\#_j$ are the global node numbers corresponding to the local node number i and j.

2.4 Newmark Schemes

The Newmark method [23] is used in the elastodynamic analysis. In the Newmark method, the global equations of motion are combined with kinematic equations of motion to solve the displacement, velocity and acceleration of the nodes. Equation (2.51) is the global equation of motion, Eqs. (2.52) and (2.53) are kinematic equations of motion. For any time step $n+1$

$$\mathbf{M}\ddot{\mathbf{d}}_{n+1}+\mathbf{C}\dot{\mathbf{d}}_{n+1}+\mathbf{K}\mathbf{d}_{n+1}=\mathbf{p}_{n+1} \tag{2.51}$$

$$\mathbf{d}_{n+1}=\mathbf{d}_n+\Delta t\dot{\mathbf{d}}_n+\frac{\Delta t^2}{2}(1-2\beta)\ddot{\mathbf{d}}_n+\frac{\Delta t^2}{2}(2\beta)\ddot{\mathbf{d}}_{n+1} \tag{2.52}$$

$$\dot{\mathbf{d}}_{n+1}=\dot{\mathbf{d}}_n+\Delta t(1-\gamma)\ddot{\mathbf{d}}_n+\Delta t\gamma\ddot{\mathbf{d}}_{n+1} \tag{2.53}$$

Several schemes in the Newmark method are available [23]. The schemes and their characteristics are listed in Table 2.2. In this thesis we implemented both the Trapezoid rule and the explicit central difference scheme to perform the dynamic structural analysis. In the following sections, the steps of carrying out these two schemes are summarized.

Table 2.2: Newmark schemes.

Scheme	Type	β	γ	Stability	Order of Accuracy
Average Acceleration (Trapezoid Rule)	Implicit	$\frac{1}{4}$	$\frac{1}{2}$	Unconditional	2
Linear Acceleration	Implicit	$\frac{1}{6}$	$\frac{1}{2}$	Conditional	2
Fox-Goodwin	Implicit	$\frac{1}{12}$	$\frac{1}{2}$	Conditional	2
Central Difference	Explicit	0	$\frac{1}{2}$	Conditional	2

2.4.1 Trapezoid rule (Implicit)

Step 1

Start from $t = 0$, $\dot{\mathbf{d}}_0$ and $\mathbf{d}_0$ are known from the initial conditions, calculate $\ddot{\mathbf{d}}_0$ by using

$$\mathbf{M}\ddot{\mathbf{d}}_0 + \mathbf{C}\dot{\mathbf{d}}_0 + \mathbf{K}\mathbf{d}_0 = \mathbf{p}_0 \tag{2.54}$$

i.e.

$$\mathbf{M}\ddot{\mathbf{d}}_0 = \mathbf{p}_0 - \mathbf{C}\dot{\mathbf{d}}_0 - \mathbf{K}\mathbf{d}_0 \tag{2.55}$$

By solving Eq. (2.55), $\ddot{\mathbf{d}}_0$ can be obtained.

Step 2

For time step = 1, substitute Eqs. (2.52,2.53) into Eq. (2.51). That is, substituting

$$\mathbf{d}_1 = \mathbf{d}_0 + \Delta t\dot{\mathbf{d}}_0 + \frac{\Delta t^2}{2}(1-2\beta)\ddot{\mathbf{d}}_0 + \frac{\Delta t^2}{2}(2\beta)\ddot{\mathbf{d}}_1 \tag{2.56}$$

and

$$\dot{\mathbf{d}}_1 = \dot{\mathbf{d}}_0 + \Delta t(1-\gamma)\ddot{\mathbf{d}}_0 + \Delta t\gamma\ddot{\mathbf{d}}_1 \tag{2.57}$$

into the equation of motion for time step 1

$$\mathbf{M}\ddot{\mathbf{d}}_1 + \mathbf{C}\dot{\mathbf{d}}_1 + \mathbf{K}\mathbf{d}_1 = \mathbf{P}_1, \tag{2.58}$$

we obtain

$$\begin{aligned} &\mathbf{M}\ddot{\mathbf{d}}_1 + \mathbf{C}\left[\dot{\mathbf{d}}_0 + \Delta t(1-\gamma)\ddot{\mathbf{d}}_0 + \Delta t\gamma\ddot{\mathbf{d}}_1\right] \\ &+\mathbf{K}\left[\mathbf{d}_0 + \Delta t\dot{\mathbf{d}}_0 + \frac{\Delta t^2}{2}(1-2\beta)\ddot{\mathbf{d}}_0 + \frac{\Delta t^2}{2}(2\beta)\ddot{\mathbf{d}}_1\right] = \mathbf{P}_1. \end{aligned} \tag{2.59}$$

Moving all the known quantities to the right-hand-side, we obtain

$$\begin{aligned} &\left(\mathbf{M} + \gamma\mathbf{C}\Delta t + \beta\Delta t^2\mathbf{K}\right)\ddot{\mathbf{d}}_1 = \\ &\mathbf{P}_1 - \left(\mathbf{C} + \Delta t\mathbf{K}\right)\dot{\mathbf{d}}_0 - \left(\Delta t(1-\gamma)\mathbf{C} + \frac{\Delta t^2}{2}(1-2\beta)\mathbf{K}\right)\ddot{\mathbf{d}}_0 - \mathbf{K}\mathbf{d}_0. \end{aligned} \tag{2.60}$$

By solving Eq. (2.60), $\ddot{\mathbf{d}}_1$ can be obtained.

Step 3

Substituting $\mathbf{d}_0$, $\dot{\mathbf{d}}_0$, $\ddot{\mathbf{d}}_0$ and $\ddot{\mathbf{d}}_1$ into Eqs. (2.52,2.53), $\mathbf{d}_1$ and $\dot{\mathbf{d}}_1$ can be calculated.

Steps 2 and 3 complete the calculation of the displacement, velocity and acceleration for time step 1. The solutions for time steps 2, 3, ..., can be obtained in the same fashion by repeating the steps 2 and 3.

2.4.2 Central or Finite difference (Explicit)

Central difference method is an explicit method with $\beta = 0$ and $\gamma = 1/2$. Note that, the central difference scheme is explicit only when $\mathbf{M}$ and $\mathbf{C}$ are diagonal matrices. Given that $\beta = 0$ and $\gamma = 1/2$, we obtain from Eqs. (2.52,2.53),

$$\mathbf{d}_{n+1} = \mathbf{d}_n + \Delta t \dot{\mathbf{d}}_n + \frac{\Delta t^2}{2} \ddot{\mathbf{d}}_n \tag{2.61}$$

$$\dot{\mathbf{d}}_{n+1} = \dot{\mathbf{d}}_n + \frac{\Delta t}{2} \ddot{\mathbf{d}}_n + \frac{\Delta t}{2} \ddot{\mathbf{d}}_{n+1} \tag{2.62}$$

Substituting Eqs. (2.61,2.62) into Eq. (2.51), we have

$$\mathbf{M}\ddot{\mathbf{d}}_{n+1} + \mathbf{C}\left(\dot{\mathbf{d}}_n + \frac{\Delta t}{2}\ddot{\mathbf{d}}_n + \frac{\Delta t}{2}\ddot{\mathbf{d}}_{n+1}\right) + \mathbf{K}\left(\mathbf{d}_n + \Delta t \dot{\mathbf{d}}_n + \frac{\Delta t^2}{2}\ddot{\mathbf{d}}_n\right) = \mathbf{P}_{n+1} \tag{2.63}$$

Rearrange the equation, we obtain

$$\left(\mathbf{M} + \frac{\Delta t}{2}\mathbf{C}\right)\ddot{\mathbf{d}}_{n+1} = \mathbf{P}_{n+1} - \mathbf{C}\left(\dot{\mathbf{d}}_n + \frac{\Delta t}{2}\ddot{\mathbf{d}}_n\right) - \mathbf{K}\left(\mathbf{d}_n + \Delta t \dot{\mathbf{d}}_n + \frac{\Delta t^2}{2}\ddot{\mathbf{d}}_n\right) \tag{2.64}$$

If $\mathbf{M}$ and $\mathbf{C}$ are diagonal, $\ddot{\mathbf{d}}_{n+1}$ can be computed from Eq. (2.64) without solving a linear system. This process is repeated until the stopping condition is fulfilled.

2.5 Computational Process

The FEA processes for both the static and dynamic analysis are summarized in Algorithms 1 and 2. The flow chart for elastodynamic analysis is shown in Figure 2.4. Note that the elastostatic FEA algorithm is only a simple subset of the elastodynamic analysis.

Algorithm 1 The Dynamic FEA Process

```
Mesh the structure.
Compute and assemble the stiffness matrix $\mathbf{K}$.
Compute and assemble the mass matrix $\mathbf{M}$.
Compute damping matrix $\mathbf{C}$.
Compute and assemble force vector.
Use Newmark method to solve the equations of motion for the displacement.
If the force is static, repeat 6 until equilibrium is reached.
If the force is dynamic, repeat 5 and 6 for every time step .
```

Algorithm 2 The Static FEA Process

```
Mesh the structure .
Compute and assemble the stiffness matrix $\mathbf{K}$.
Compute and assemble Force Vector.
Apple boundary conditions.
Solve (2.34) for steady state displacement.
```

2.6 Numerical Results

We have tested our code with numerous test cases and validated our code. In this section, we present numerical results of several examples and compare our results with those obtained in ANSYS.

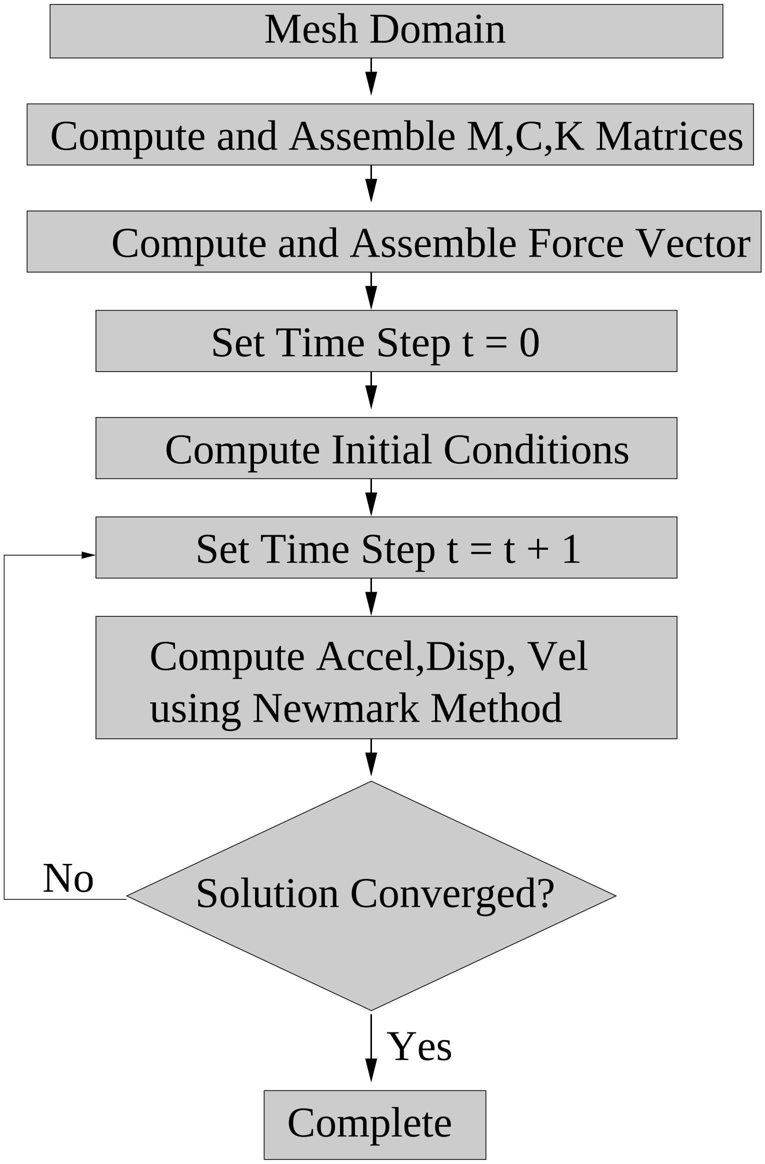

Figure 2.4: Flow Chart for 3D Dynamic FEA

2.6.1 Static Analysis of a Cantilever Plate

The first example is a 8×8 cm cantilever plate with a thickness of 1 cm subjected to a pressure of 0.1 Pa. The Young's modulus of the material is 10 MPa. The Poisson's ratio is 0.25. The plate is meshed with $10 \times 10 \times 3$ 8-node brick elements in ANSYS. This test problem is solved in ANSYS as well as in our solver. Figure 2.5 shows the deformation of the plate obtained from our solution. Table 2.3 shows a comparison of the nodal displacement solution for the first 10 nodes given by ANSYS and the results obtained from our code. The results obtained from ANSYS and our code are identical.

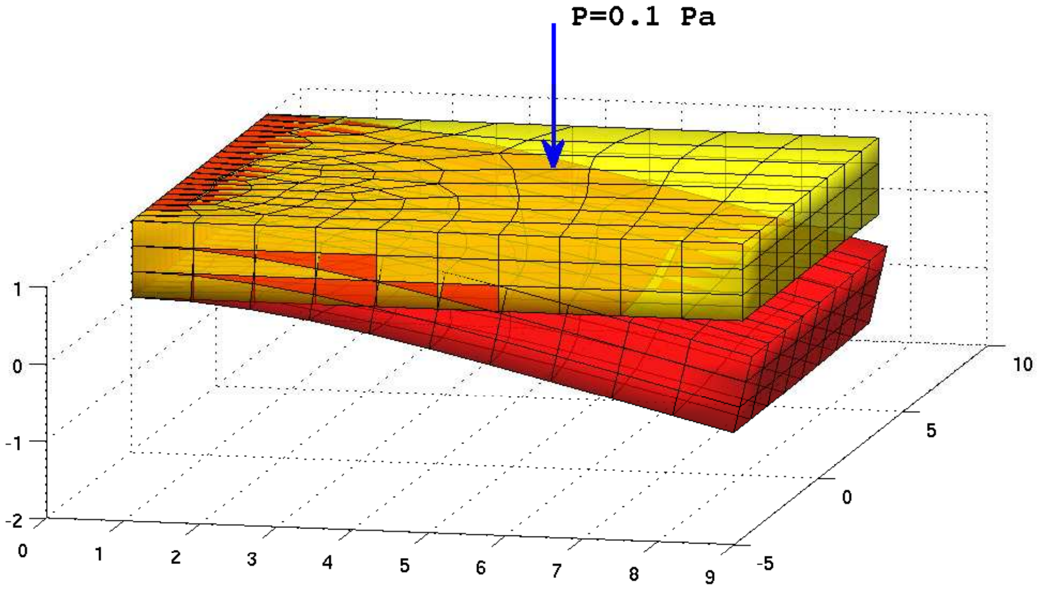

Figure 2.5: A cantilever plate subjected a pressure.

Table 2.3: ANSYS vs. FEA solver: cantilever plate subjected to a uniform pressure.

Node #	FEA Solver			ANSYS		
	x (cm)	y (cm)	z (cm)	x (cm)	y (cm)	z (cm)
1	0.000000	0.000000	0.000000	0.0000	0.0000	0.0000
2	-0.039906	0.000026	-0.486716	-0.39906E-01	0.25695E-04	-0.48672
3	-0.010336	-0.003006	-0.007782	-0.10336E-01	-0.30061E-02	-0.77816E-02
4	-0.019168	-0.002744	-0.032585	-0.19168E-01	-0.27443E-02	-0.32585E-01
5	-0.026275	-0.002862	-0.069768	-0.26275E-01	-0.28615E-02	-0.69768E-01
6	-0.031644	-0.002471	-0.117437	-0.31644E-01	-0.24713E-02	-0.11744
7	-0.035371	-0.001887	-0.172446	-0.35371E-01	-0.18872E-02	-0.17245
8	-0.037746	-0.001304	-0.232169	-0.37746E-01	-0.13045E-02	-0.23217
9	-0.039085	-0.000785	-0.294640	-0.39085E-01	-0.78466E-03	-0.29464
10	-0.039699	-0.000364	-0.358438	-0.39699E-01	-0.36399E-03	-0.35844

2.6.2 Static Analysis of Mirror C

In the second example, we perform a static analysis on Mirror C shown in Chapter 1. A point force is applied to a corner of the mirror plate as shown in Figure 2.6. The material properties of the mirror structure is listed in Table 1.1. The mirror is meshed with 3849 8-node brick elements in ANSYS. The total number of nodes is 6008 resulting in 18024 degrees of freedom. This test problem is solved in ANSYS as well as in our solver. Figure 2.6 shows the deformation of the mirror structure obtained from our solution. Table 2.4 shows a comparison of the nodal displacement solution for the first 10 nodes given by ANSYS and the results obtained from our code. The results obtained from ANSYS and out code are identical.

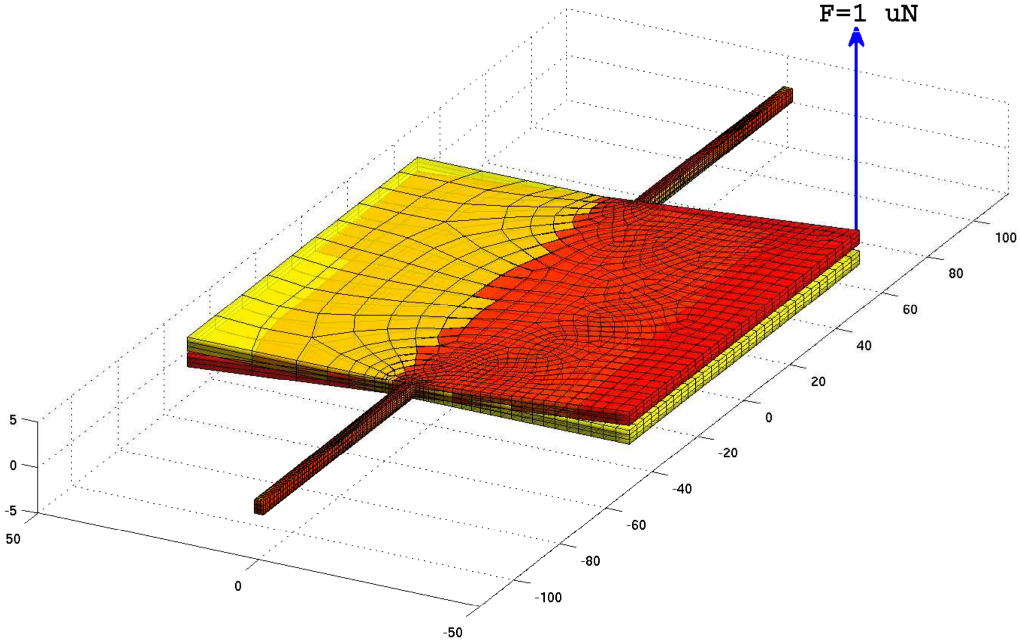

Figure 2.6: Static analysis: Mirror C.

Table 2.4: ANSYS vs. FEA Solver: Mirror C subjected to a point force.

Node #	ANSYS			FEA Solver		
	x(μm)	y(μm)	z(μm)	x(μm)	y(μm)	z(μm)
1	0.000812	-0.014614	1.126587	0.81151E-03	-0.14614E-01	1.1266
2	0.000436	-0.014472	0.272161	0.43586E-03	-0.14472E-01	0.27216
3	0.000800	-0.014611	1.087989	0.79951E-03	-0.14611E-01	1.0880
4	0.000779	-0.014605	1.048469	0.77934E-03	-0.14606E-01	1.0485
5	0.000762	-0.014603	1.008009	0.76210E-03	-0.14603E-01	1.0080
6	0.000746	-0.014602	0.966576	0.74640E-03	-0.14602E-01	0.96658
7	0.000730	-0.014600	0.924146	0.72962E-03	-0.14600E-01	0.92415
8	0.000711	-0.014595	0.880702	0.71125E-03	-0.14595E-01	0.88070
9	0.000692	-0.014589	0.836225	0.69216E-03	-0.14589E-01	0.83622
10	0.000673	-0.014583	0.790693	0.67326E-03	-0.14583E-01	0.79069

2.6.3 Modal Analysis of Mirror A/B

In the third example, we perform a modal analysis on Mirror A or B (Mirror A and B have the same mirror structure). In this example, the mirror is meshed with 646 8-node brick elements in ANSYS. The total number of nodes is 1302 resulting in 3906 degrees of freedom. This test problem is solved in ANSYS as well as in our solver. Tables 2.5 and 2.6 list the first 10 natural frequencies of the mirror. Once again, the results obtained by ANSYS (not shown) and the results obtained from our code are identical. Figure 2.7 shows the first 10 vibrational modes of the mirror. It is shown that the first mode is a rotational mode, the second mode is a bending mode and the third mode is a twisting mode. For the first mode, the natural frequency is 0.0474 MHz which is corresponding to a period of 21.1 μs. For the second mode, the frequency is 0.125670 MHz with a period of 8 μs. Compared to the first frequency, the second frequency is about 2.65 times larger.

Table 2.5: Natural frequencies of Mirror A/B.

Mode	1	2	3	4	5
Frequency (MHz)	0.047398	0.125670	0.136935	0.246021	0.316886

Table 2.6: Natural frequencies of Mirror A/B.

Mode	6	7	8	9	10
Frequency (MHz)	1.473245	3.440778	3.483548	3.595135	4.884864

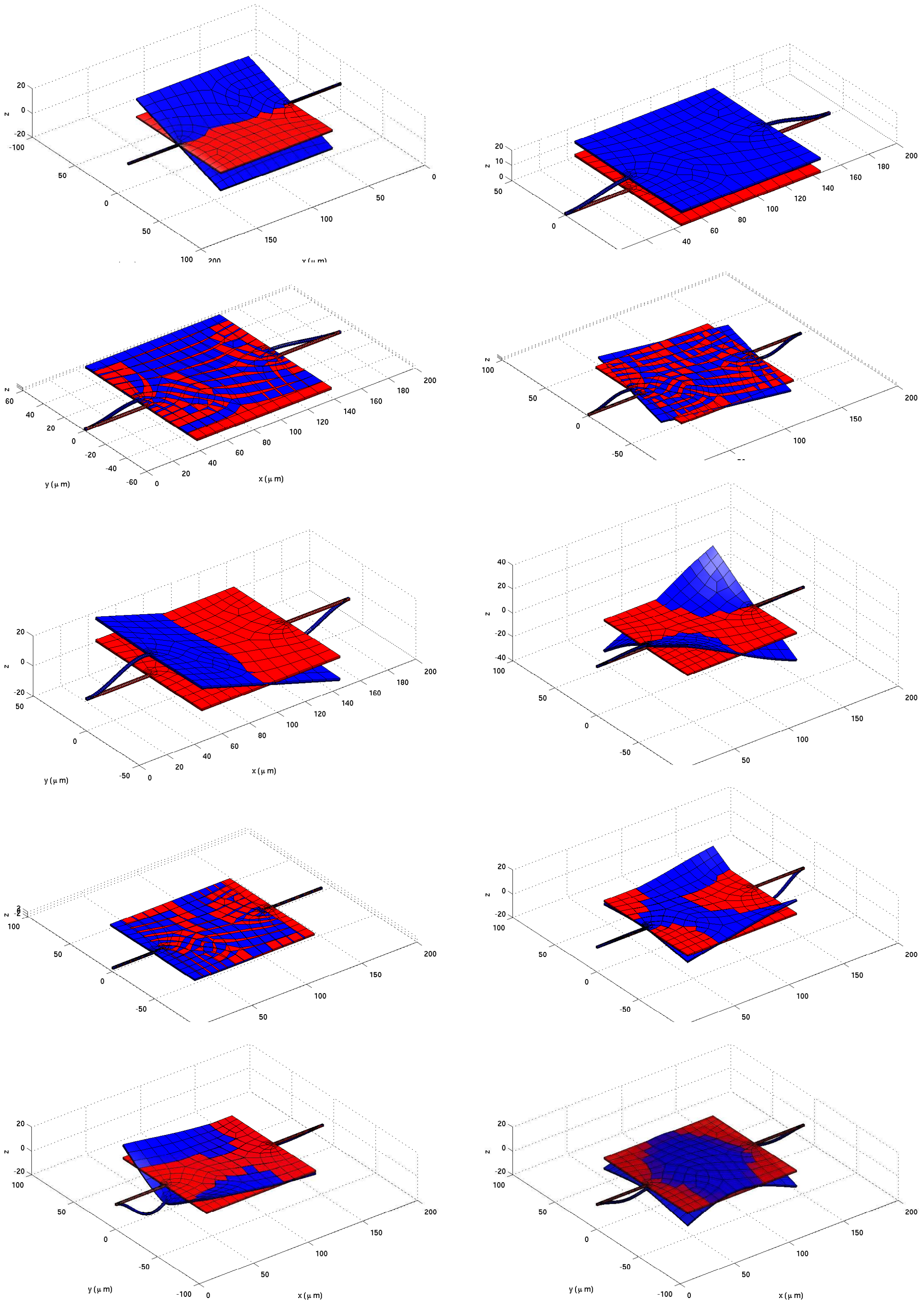

Figure 2.7: Vibrational modes of Mirror A/B.

2.6.4 Dynamic Analysis of Micromirror

In the fourth example, we perform a free vibration dynamic analysis on Mirror A/B. The first three modes are taken as the initial displacement of the structure. Then the structure is set free for vibration. Our dynamics code computes the time history of the free vibration. In this example, the damping is set to zero. Figure 2.8 shows the displacement of a corner of the mirror plate as a function of time. Periodic movement of the structure is obtained as expected. As shown in the figures, the frequencies of the three free vibrations are approximately 0.047 MHz, 0.126 MHz and 0.137 MHz. These results match the frequencies obtained from the modal analysis.

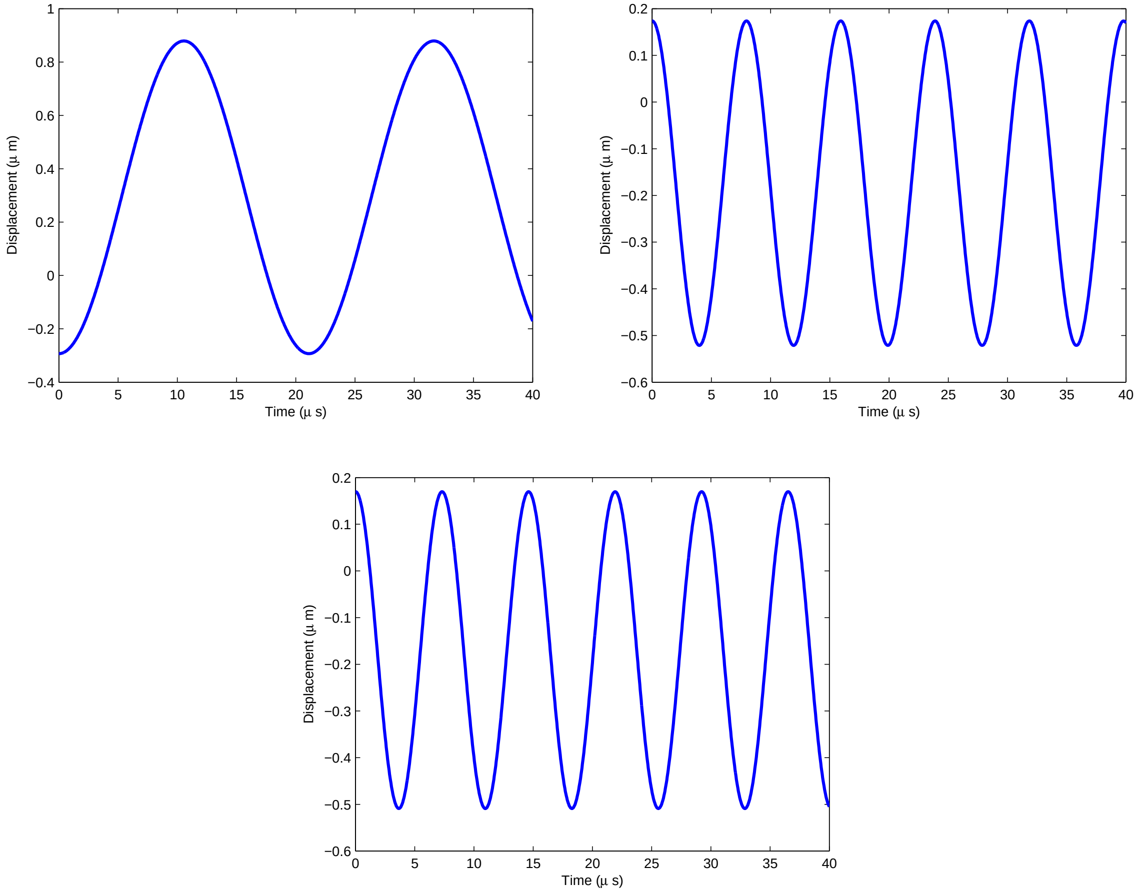

Figure 2.8: Dynamic peak displacement of Mirror A/B.

Chapter 3

Boundary Element Method for Electrostatic Analysis

3.1 Mathematical Model

Consider two conductors as shown in Figure 3.1, the goal of the electrostatic analysis using the boundary element method (BEM), is to determine the charge density of each of the conductors based on the potential difference between the two. The governing equation

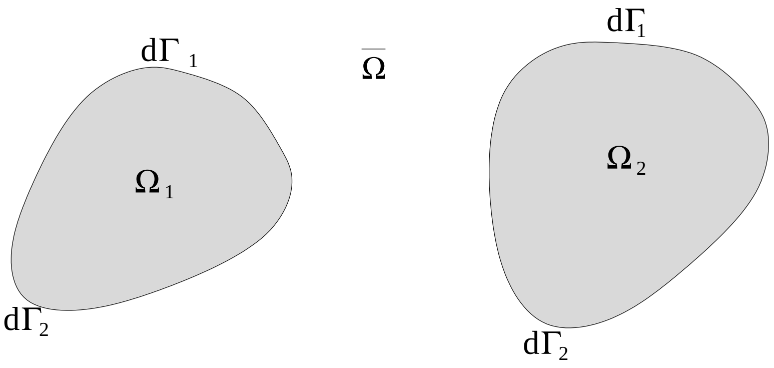

Figure 3.1: Domain of boundary element method.

for electrostatic analysis is Laplace's Equation which can be written as[26]

$$\nabla^2 u = 0 \text{ in } \bar{\Omega} \tag{3.1}$$

with boundary conditions

$$u = \bar{u} \text{ on } \Gamma_1 \tag{3.2}$$

$$q = \frac{\partial u}{\partial \mathbf{n}} = \bar{q} \text{ on } \Gamma_2 \tag{3.3}$$

where $\bar{\Omega}$ is the domain exterior to Ω_1 and Ω_2, u is the voltage applied to the conductors (i.e., electric potential), and $\mathbf{n}$ is the normal of the boundary. Either the potential or the charge density are known for each point on the boundary. In electrostatics the voltage is always known and the surface charge density will be computed. An efficient approach to treat exterior electrostatic problems is to use a boundary integral equation [26,27]. A boundary integral equation for the electrostatic problem is given by [28],

$$u(P) = \int_\Gamma G(P,Q) q(Q) d\Gamma + C \tag{3.4}$$

$$\int_\Gamma q(Q) d\Gamma = C_T \tag{3.5}$$

where q is the unknown normal derivative of u, P is the source point, Q is the field point, $G(P,Q)$ is the Green's function and $\Gamma = d\Gamma_1 \cup d\Gamma_2$. In three-dimensions,

$$G(P,Q) = \frac{1}{4\pi r(P,Q)} \tag{3.6}$$

where $r(P,Q)$ is the distance between the source point and the field point, C_T is the total charge of the system (typically set to be zero) and C is an unknown variable which needs to be computed. Note that the variables in the boundary-integral equations (3.4), (3.5) are written with respect to the deformed positions of the conductors.

3.2 Discretization and Approximation

The conductors are discretized into surface elements. For our case we used the surface elements from the FEA mesh so that the nodes for the FEA and BEM will match and no interpolation will be needed. We use constant elements for BEM so that each element will have only one node at its centroid as shown in Figure (3.2). The centroid of each element is taken as the collocation point and the value of the potential and its normal gradient at the collocation point represent the value of the potential and its normal gradient on the element. For the case of the micro-mirror, only the face of the mirror plate nearest the electrode and the face of the electrode nearest the plate are used for the analysis. This is due to the fact that the charges gather at the surfaces of these two structures at the points that are closest to the other structure. The surface charge density is concentrated on these surfaces. The charge density of the rest of the mirror is negligible. The boundary integral

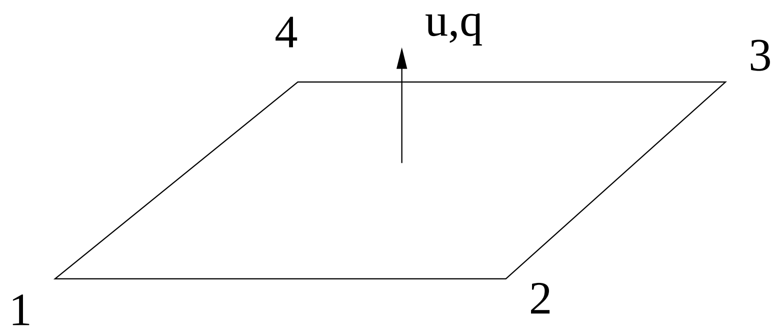

Figure 3.2: Constant Boundary element.

equation for a source point P can be written as

$$u(P) = \sum_{k=1}^{K} \int_{\Gamma_k} \frac{1}{4\pi r(P, Q_k)} q(Q_k) d\Gamma + C \tag{3.7}$$

$$\sum_{k=1}^{K} \int_{\Gamma_k} q(Q_k) d\Gamma = C_T \tag{3.8}$$

where K is the number of elements, Γ_k is the area of the kth element, Q_k is the field point on the kth element and $q(Q_k)$ is the unknown for the k-th element. Equations (3.7-3.8) can be rewritten in a matrix form as

$$\mathbf{M}\mathbf{q} = \mathbf{u} \tag{3.9}$$

where $\mathbf{M}$ is a $(K+1) \times (K+1)$ coefficient matrix, $\mathbf{u}$ and $\mathbf{q}$ are the $(K+1) \times 1$ right hand side and unknown vectors, respectively. The entries in the coefficient matrix are given by

$$\begin{cases} M(i,j) = \int_{\Gamma_j} \frac{1}{4\pi r(P_i, Q_j)} d\Gamma & i,j = 1,\ldots,K \\ M(K+1,j) = \int_{\Gamma_j} d\Gamma & j = 1,\ldots,K \\ M(i,K+1) = 1 & i = 1,\ldots,K \\ M(K+1,K+1) = 0 & \end{cases} \tag{3.10}$$

$$\mathbf{u} = \left\{ \begin{array}{c} u_1 \\ u_2 \\ \cdot \\ \cdot \\ \cdot \\ u_K \\ C_T \end{array} \right\} \qquad \mathbf{q} = \left\{ \begin{array}{c} q_1 \\ q_2 \\ \cdot \\ \cdot \\ \cdot \\ q_K \\ C \end{array} \right\} \tag{3.11}$$

The $\mathbf{u}$ vector in Eq. (3.11) is known from the potential boundary conditions. The unknown vector of surface normal derivative of potential in Eq. (3.11) can be computed by solving the matrix problem in Eq. (3.9). Note that, the electric field E normal to the surface is given by

$$E = -q \tag{3.12}$$

3.3 Singular Integration

A numerical integration technique needs to be employed to compute M. Before the integration, the boundary elements are mapped to 2D isoparametric elements. For the cases where $i \neq j$ a regular Gaussian quadrature can be used. For the cases where $i = j$ the integration becomes singular. Special integration techniques is required. There are three popular methods for dealing with singular integrals, the weighted Gauss integration, the transformation of variable technique, and the partial analytical Taylor series expansion technique [30,31]. The weighted Gauss method is not recommended by many authors due to its many limitations, therefore only the later two methods are discussed here in detail.

The transformation technique divides the element into triangular sub-elements then transforms the triangular element to a square plane[30]. Due to the fact that we use constant elements, the singularity points are in the center of the cells. The element is split into four triangular sub-cells. Each of these sub-cells is mapped to an isoparametric triangular element. The shape functions for the triangular isoparametric element are shown in Eq. (3.13), the corresponding element is shown in Figure (3.3 (c)).

$$\begin{aligned} N_1(\xi,\eta) &= \frac{1}{2}(1-\xi) \\ N_2(\xi,\eta) &= \frac{1}{2}(\xi-\eta) \\ N_3(\xi,\eta) &= \frac{1}{2}(1+\eta) \end{aligned} \tag{3.13}$$

Equation (3.10) can be rewritten for each triangle as:

$$\int_{-1}^{1}\int_{-\xi}^{1} \frac{J(\xi,\eta)}{4\pi r[P,Q(\xi,\eta)]} d\xi d\eta \tag{3.14}$$

where $J(\xi,\eta)$ is the Jacobian of the transformation from the triangular sub-element to the isoparametric triangular element, and $r[P,Q(\xi,\eta)]$ is the distance from the source point to the field point. The Jacobian $J(\xi,\eta)$ can be computed as

$$J(\xi,\eta) = det\left|\begin{bmatrix} \frac{\partial N_1(\xi,\eta)}{\partial\xi} & \frac{\partial N_2(\xi,\eta)}{\partial\xi} & \frac{\partial N_3(\xi,\eta)}{\partial\xi} \\ \frac{\partial N_1(\xi,\eta)}{\partial\eta} & \frac{\partial N_2(\xi,\eta)}{\partial\eta} & \frac{\partial N_3(\xi,\eta)}{\partial\eta} \end{bmatrix}\begin{bmatrix} x_1 & y_1 \\ x_2 & y_2 \\ x_3 & y_3 \end{bmatrix}\right| \tag{3.15}$$

where N_i, $i = 1,2,3$, are the shape functions given in Eq. (3.13). The following transformation of variables is then used on the isoparametric triangular element to map it to a square element as shown in Figure (3.3 (d)).

$$\begin{aligned} u &= \xi \\ v &= \frac{1-\xi+2\eta}{1+\xi} \end{aligned} \tag{3.16}$$

the Jacobian for this transformation is

$$J^s = \frac{1+u}{2}. \tag{3.17}$$

Equation (3.14) can now be written as

$$\frac{1}{2}\int_{-1}^{1}\int_{-1}^{1}\frac{J(\xi,\eta)(1+u)}{4\pi r[P,Q(\xi,\eta)]}dudv \tag{3.18}$$

where, from Eq. (3.16)

$$\begin{aligned} &\xi = u \\ &\eta = \frac{(1+u)(1+v)}{2} - 1 \end{aligned} \tag{3.19}$$

Substituting Eq. (3.19) into Eq. (3.18) and carrying out the Gaussian quadrature on Eq. (3.18) gives

$$\frac{1}{2}\int_{-1}^{1}\int_{-1}^{1}\frac{J(u,v)(1+u)}{4\pi r[P,Q(u,v)]}dudv \approx \frac{1}{2}\sum_{g=1}^{NG}\frac{J(u_g,v_g)(1+u_g)}{4\pi r[P,Q(u_g,v_g)]}w_g \tag{3.20}$$

where NG is the number of Gauss points and w_g is the weight.

The Taylor expansion method for evaluating weakly singular integrals involves expanding the integrand by use of Taylor Series and subtracting out the singularity. Also, a corresponding term will be added which can be integrated analytically . The integration

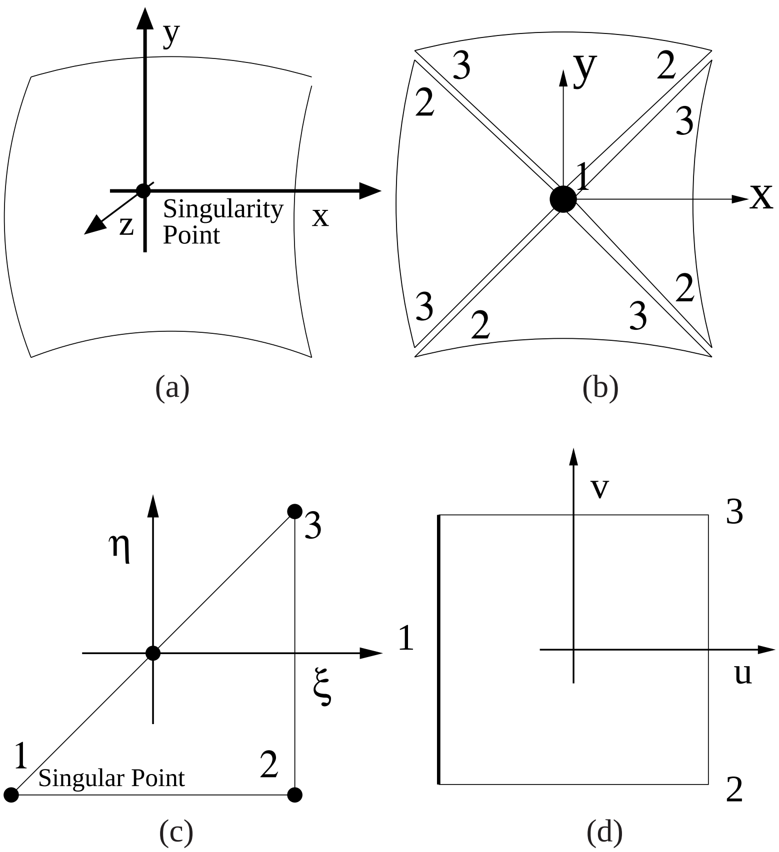

Figure 3.3: Transformation of Variable Technique Procedure

technique can be written as [31]

$$\begin{aligned}\int_{-1}^{1}\int_{-1}^{1}\frac{J(\xi,\eta)}{4\pi r[P,Q(\xi,\eta)]}d\xi d\eta &= \int_{-1}^{1}\int_{-1}^{1}\left(\frac{J}{4\pi r}\right)_3 d\xi d\eta \\ &\quad+\int_{-1}^{1}\int_{-1}^{1}\left(\frac{J}{4\pi r}-\left(\frac{J}{4\pi r}\right)_3\right)d\xi d\eta \qquad (3.21)\end{aligned}$$

where $N(\xi,\eta)$ is the shape functions for the element, $J(\xi,\eta)$ is the Jacobian for the mapping to the isoparametric element, and $\left(\frac{MJ}{R}\right)_3$ is the third order Taylor's Expansion of the original integrand. In this work, we adopt the transformation method for the singular integration where 6×6 Gauss points are used in the square element in $u - v$ coordinate system.

The application of boundary conditions is straightforward. The values for the voltage are simply applied to the collocation points, and since the voltage is constant throughout each structure, one voltage will be applied to all of the cells in Γ_1 and a different voltage will be applied to all of the cells in Γ_2. These voltages are the values that make up $\mathbf{u}$. For our case the voltage of the mirror is zero and the voltage of the electrode can vary based on the input. Algorithm 3 and Figure 3.4 summarize the electrostatic analysis process.

Algorithm 3 The electrostatic analysis process.

```
1: Mesh the structure.
2: Compute $\mathbf{M}$.
3: Apply boundary conditions.
4: Solve Eq. (3.9) for $\mathbf{q}$.
```

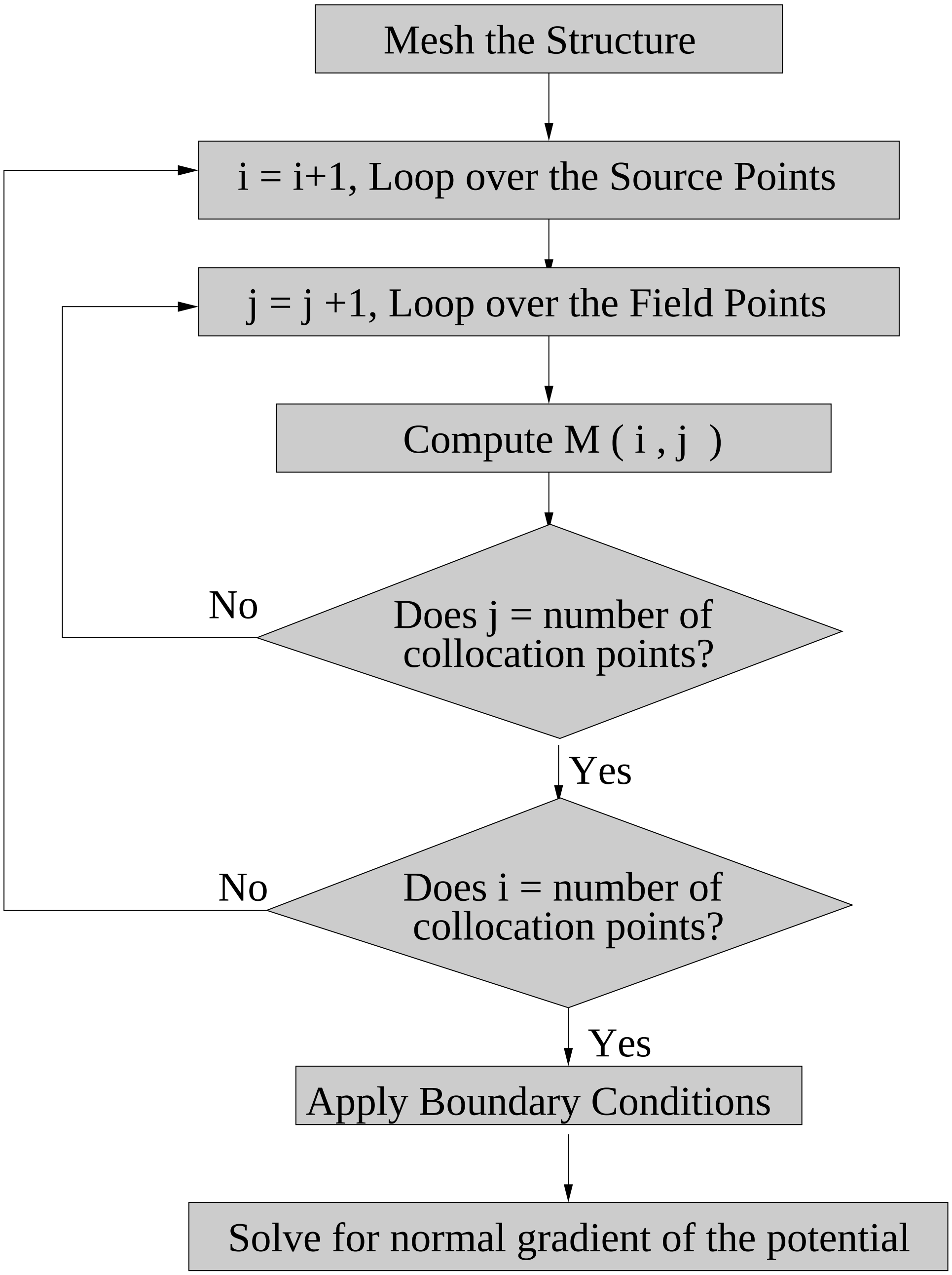

Figure 3.4: Boundary element method flow chart.

3.4 Numerical Results

We have tested our electrostatic code with numerous test cases. In this section, we present numerical results of an examples and compare our results with known exact solutions. The example is a two plate conductor system as shown in Figure 3.5. Each conductor has dimensions of $100\mu m \times 100\mu m$ and the gap between the two plates is 2 μm. The applied voltage is set to be 1 V for the upper plate and 0 V for the lower plate. Since the plate is very long compared to the gap the electric field at the center point of the plate is given by

$$E = -\frac{V_{ab}}{d} = -2V/\mu m \tag{3.22}$$

where V_{ab} is the potential difference between the two plates and d is the gap. The BEM solution is shown in Figure 3.6. The solution for the center of the plates is compared to the analytical solution. Figure 3.7 shows the convergence behavior of the BEM solution. Figure 3.8 shows the electric field between two staggered parallel plates.

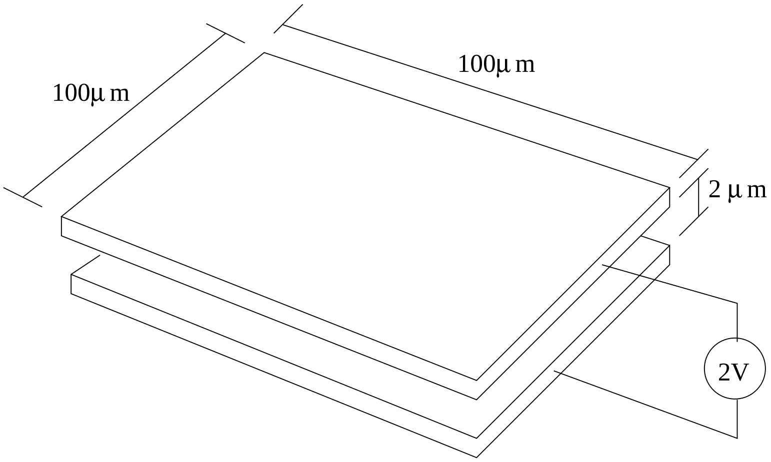

Figure 3.5: Setup of two parallel plates.

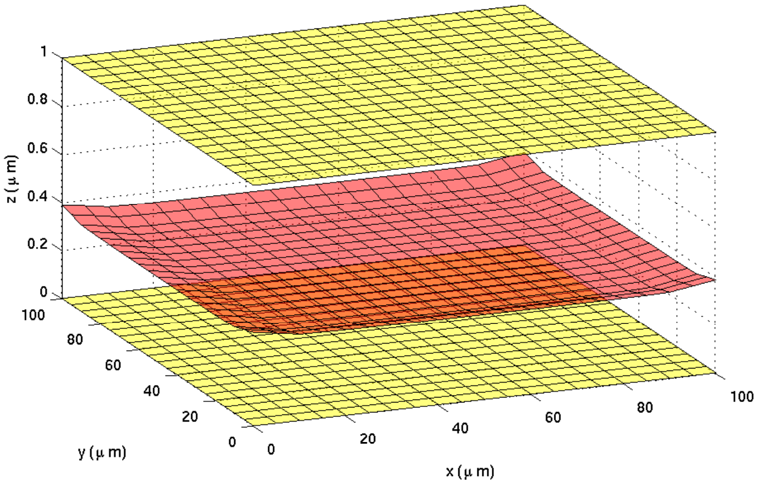

Figure 3.6: Electric field between two parallel plates.

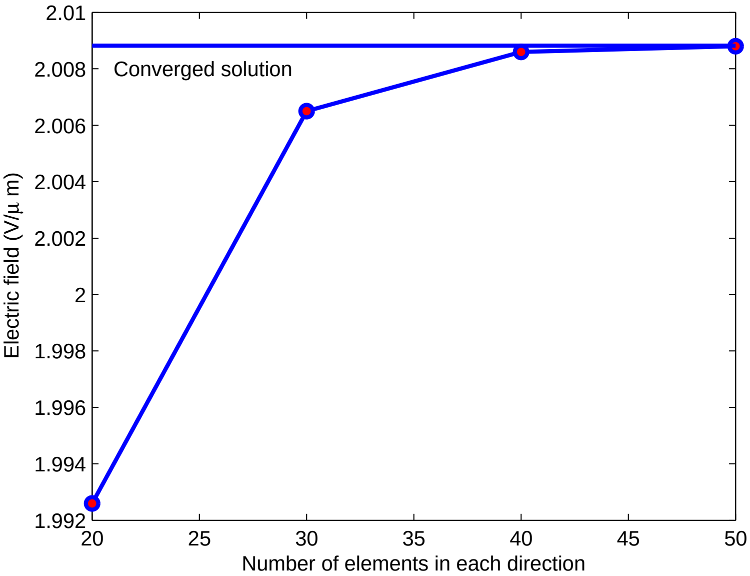

Figure 3.7: Convergence of the BEM solution.

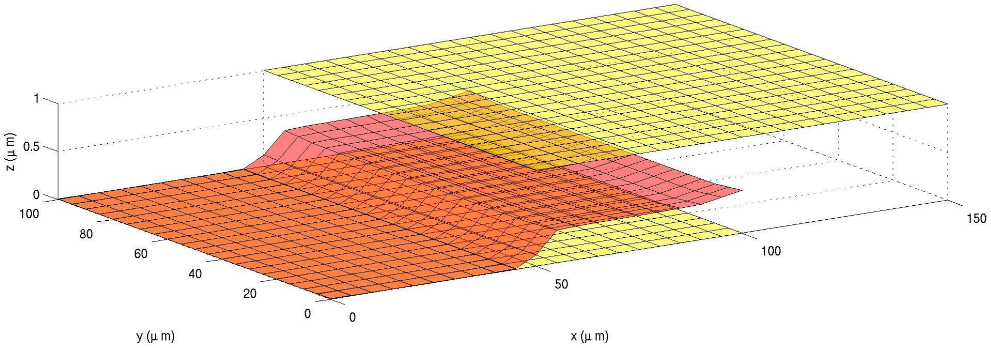

Figure 3.8: Electric field between two staggered parallel plates.

Chapter 4

Coupled Electromechanical Analysis of MEMS

4.1 Static Coupled Electromechanical Analysis

In the static coupled electro-mechanical analysis, two sets of governing equations are solved self-consistently. The equations of equilibrium are solved for the structures and the exterior electrostatic equation is solved to obtain the surface charge density. The self-consistent analysis is performed via a relaxation iteration as shown in Figure 6.1. The governing equations of equilibrium are given by

$$\mathbf{K}\mathbf{d} = \mathbf{P}. \tag{4.1}$$

where $\mathbf{P}$ is the force vector. In the electromechanical analysis, the force vector $\mathbf{P}$ contains the electrostatic surface pressure prescribed as a boundary condition. $\mathbf{P}$ is given by

$$\mathbf{P} = P_e\mathbf{N} \tag{4.2}$$

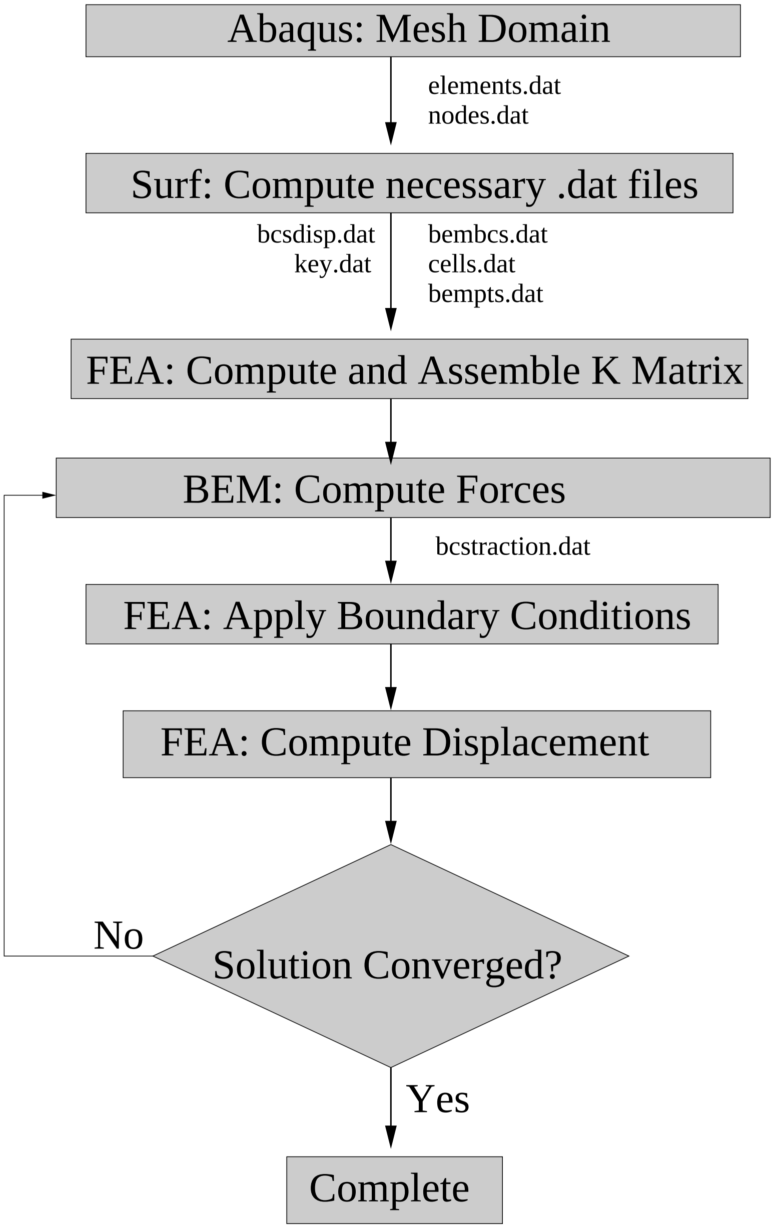

Figure 4.1: Flow chart for coupled electromechanical static solver.

where $\mathbf{N}$ is the normal vector on the surface P_e is the electrostatic pressure generated by the electric charge accumulated on the surface of the structure. P_e is computed by

$$P_e = \frac{\sigma^2}{2\epsilon} \tag{4.3}$$

where ϵ is the permittivity of free space and σ is the surface charge density. The electrostatic pressure in Eq. (4.3) is applied as the boundary condition for the mechanical analysis by using Eq. (4.2). The surface charge density is obtained by the electrostatic analysis. The governing boundary integral equations for electrostatics is given by

$$u(P) = \int_{\Gamma_Q} G(P,Q) q d\Gamma + C \tag{4.4}$$

$$\int_{\Gamma_Q} q\Gamma = 0 \tag{4.5}$$

where q is the normal gradient of the potential. Note that Eqs (4.4-4.5) are all defined in the deformed configuration. Once q is obtained, the surface charge density is computed by

$$\sigma = -\epsilon q \tag{4.6}$$

Static coupled electromechanical analysis is performed to obtain the pull-in curve for the three micromirrors shown in Chapter 1. Figure 4.2 shows the static pull-in of Mirror A. The pull-in voltage is 18.74 V. This result compares favorably with the pull-in voltage of 18.4 V obtained in [10] where the same mirror was investigated. Figure 4.3 shows the static pull-in of Mirror B. The pull-in voltage is 27.4 V. While Mirror A and Mirror B have the same dimensions, the positions of the electrodes are different. The electrodes of Mirror B is closer to the center of the mirror plate. It is shown from the results that the position of the electrodes can change the pull-in voltage significantly. Figure 4.4 shows the static pull-in of Mirror C. The pull-in voltage is 23.5 V. In this case, although the electrodes are placed close to the center of the mirror plate, the suspension beams are longer than those of Mirror A and B. As longer beams have lower bending stiffness, the pull-in voltage becomes lower. The results of the static coupled analysis show that the pull-in voltage is a function of both the stiffness of the beam and the position of the electrodes. Figure 4.5 shows the deformed shape of the Mirror C subjected to the electrostatic force. Figure 4.6 shows the distribution of the surface charge density on the surface of the mirror and electrodes.

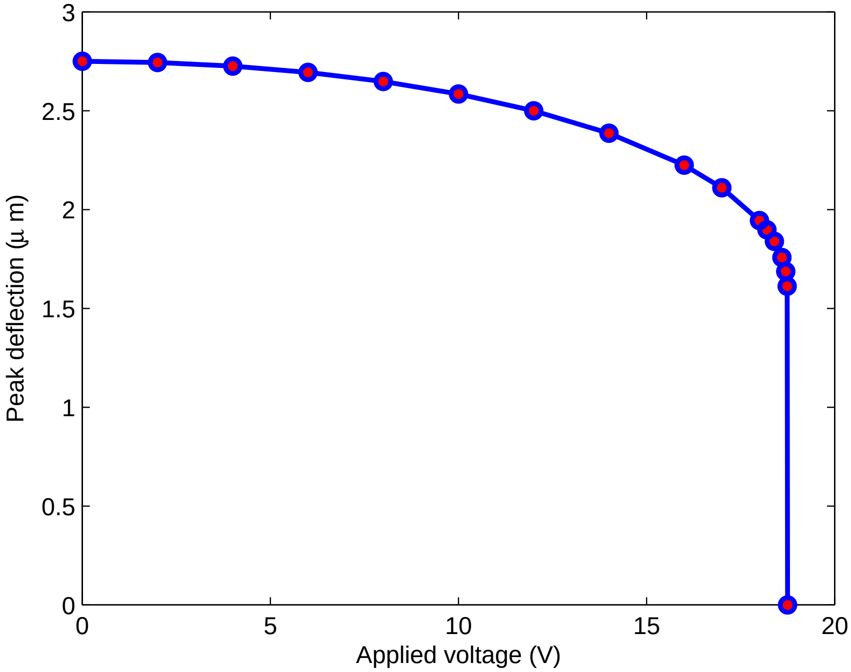

Figure 4.2: Static pull-in of Mirror A.

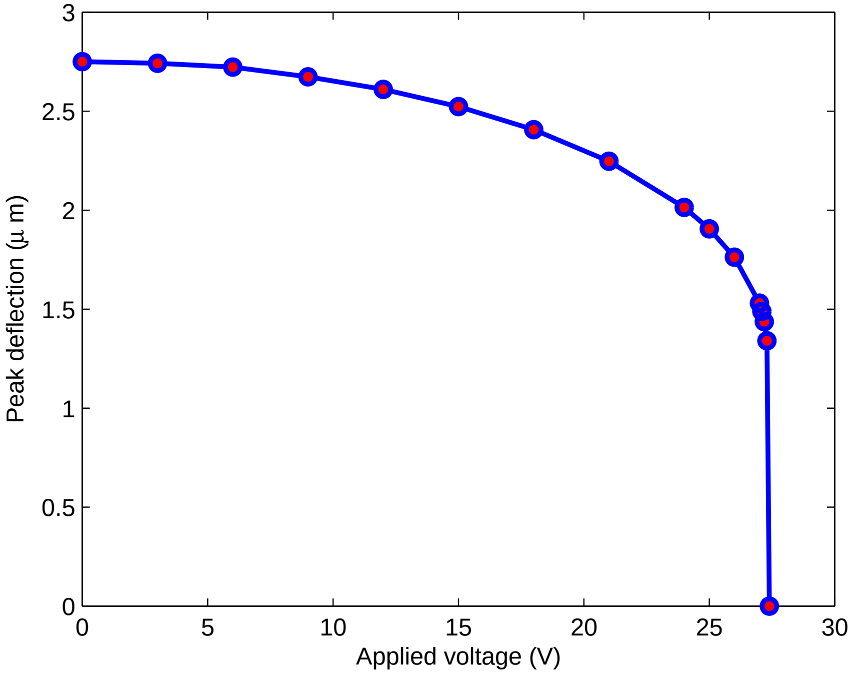

Figure 4.3: Static pull-in of Mirror B.

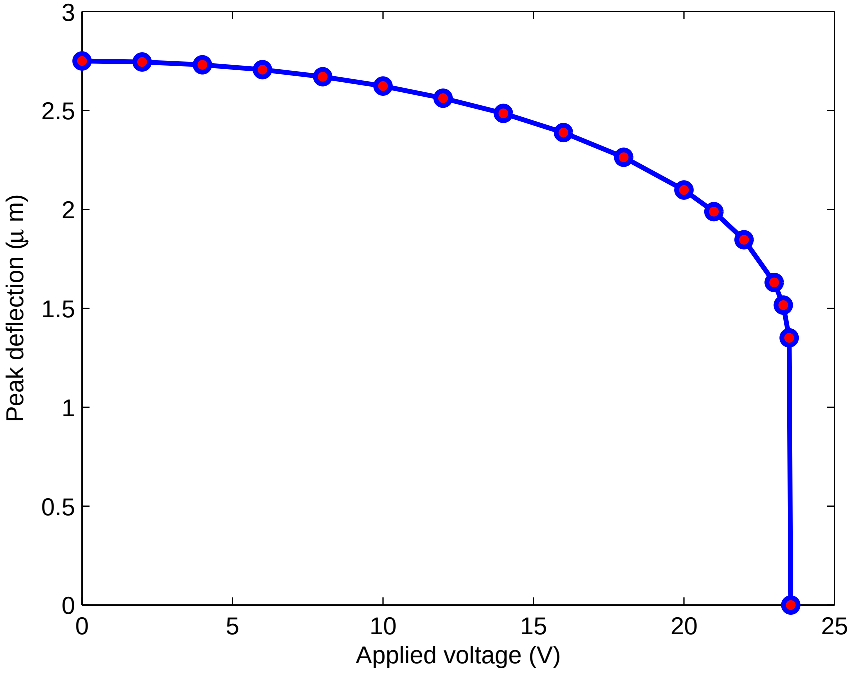

Figure 4.4: Static pull-in of Mirror C.

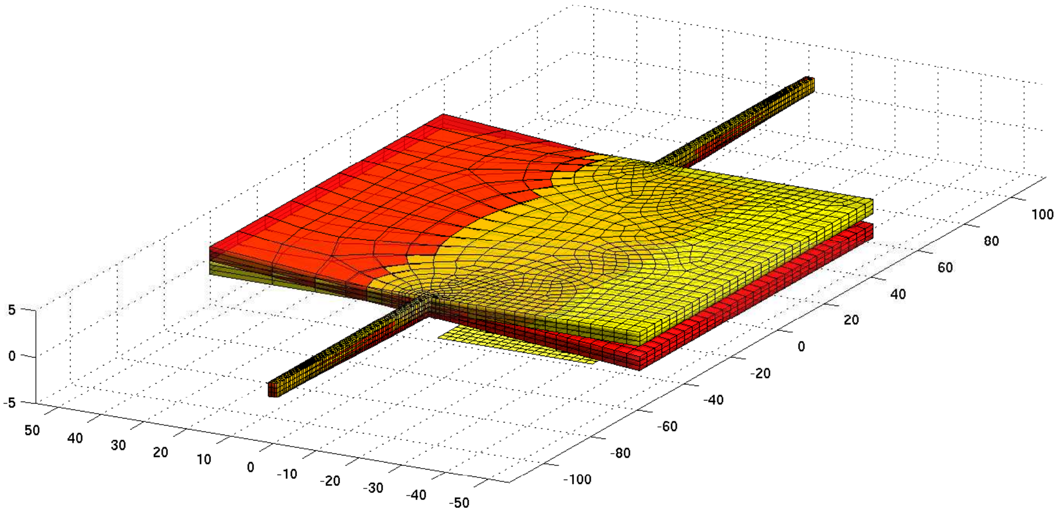

Figure 4.5: Deformation of Mirror C due to electrostatic pressure.

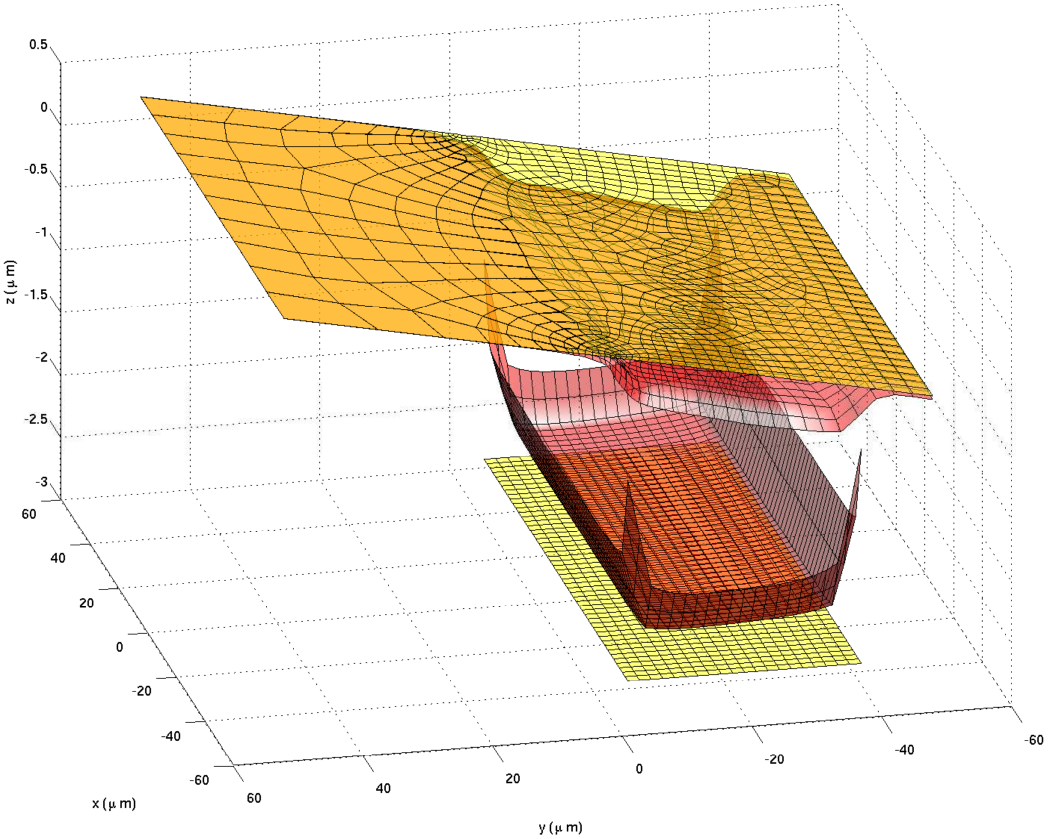

Figure 4.6: Surface charge density distribution on the mirror plate and the electrode.

4.2 Dynamic Coupled Electromechanical Analysis

In the dynamic coupled electro-mechanical analysis, the equations of motion are solved for the structures and the exterior electrostatic equation is solved to obtain the surface charge density. Within each time step, the mechanical domain and electrostatic domain are solved self-consistently. The flow chat of the dynamic electromechanical analysis is shown in Figure 4.7.

Different from the static coupled analysis, for a given time step $n+1$, the following governing equations are to be satisfied simultaneously:

$$\mathbf{M}\ddot{\mathbf{d}}_{n+1} + \mathbf{C}\dot{\mathbf{d}}_{n+1} + \mathbf{K}\mathbf{d}_{n+1} = \mathbf{P}_{n+1}. \tag{4.7}$$

$$\mathbf{P}_{n+1} = P_{e_{n+1}}\mathbf{N}_{n+1} \tag{4.8}$$

$$P_{e_{n+1}} = \frac{\sigma_{n+1}^2}{2\epsilon} \tag{4.9}$$

$$u_{n+1}(P) = \int_{\Gamma_Q} G(P,Q) q_{n+1} d\Gamma + C \tag{4.10}$$

$$\int_{\Gamma_Q} q_{n+1}\Gamma = 0 \tag{4.11}$$

$$\sigma_{n+1} = -\epsilon q_{n+1} \tag{4.12}$$

Within the time step, the relaxation iterations are performed to obtain a convergent solution between the mechanical and electrostatic domains. Once a convergent solution is obtained, the solution procedure moves to the next time step by using the Newmark method.

Figure 4.2 shows the dynamic response of Mirror C with an applied voltage of 20 V. When the beam moves down due to the electrostatic force, the nonlinear electrostatic force becomes larger and slows down the vibrational movement of the mirror. It is shown in the figure that the vibration frequency of the mirror is lower when it deforms close to the electrode. When the applied voltage is increased, the mirror stays at the bottom

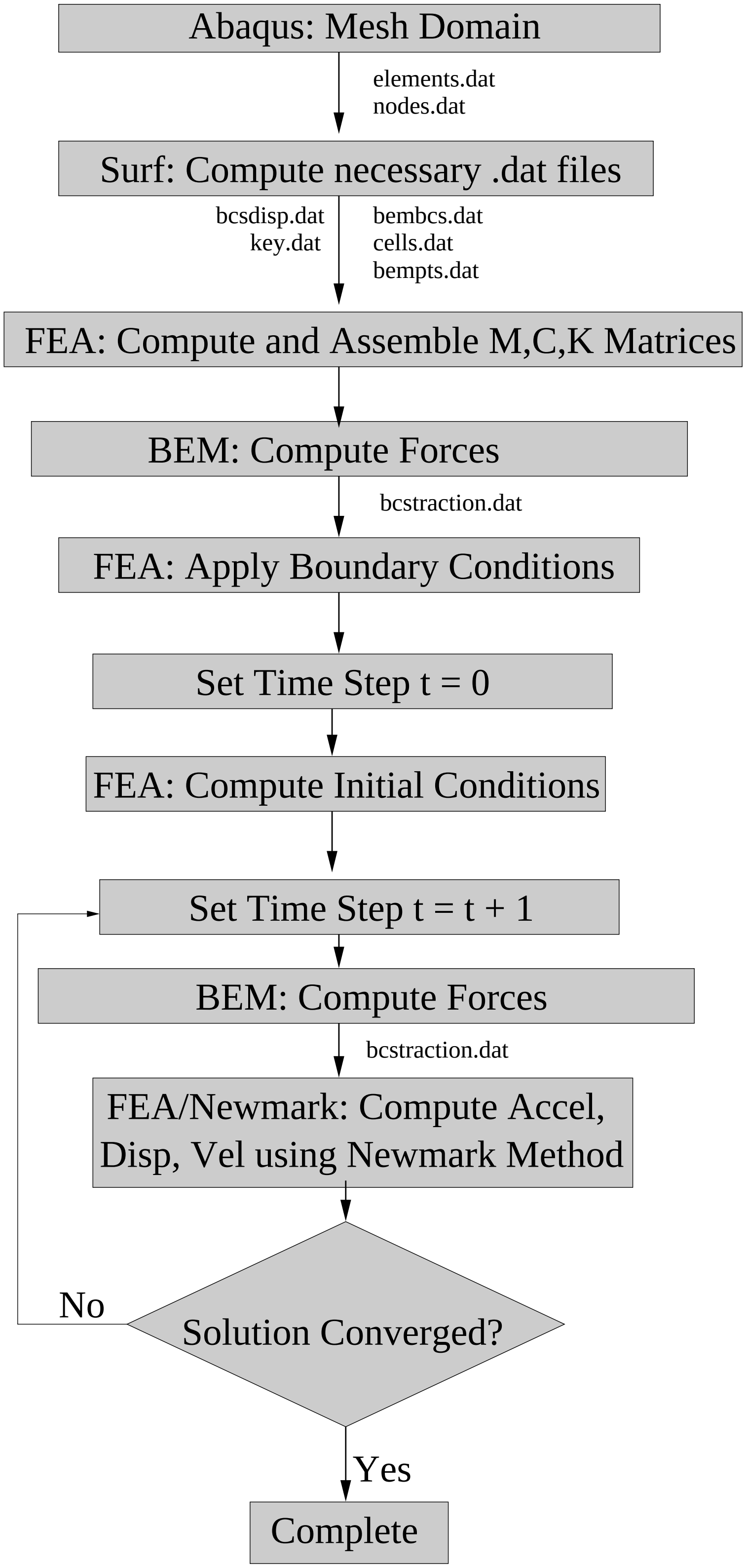

Figure 4.7: Flow chart for dynamic coupled electromechanical analysis.

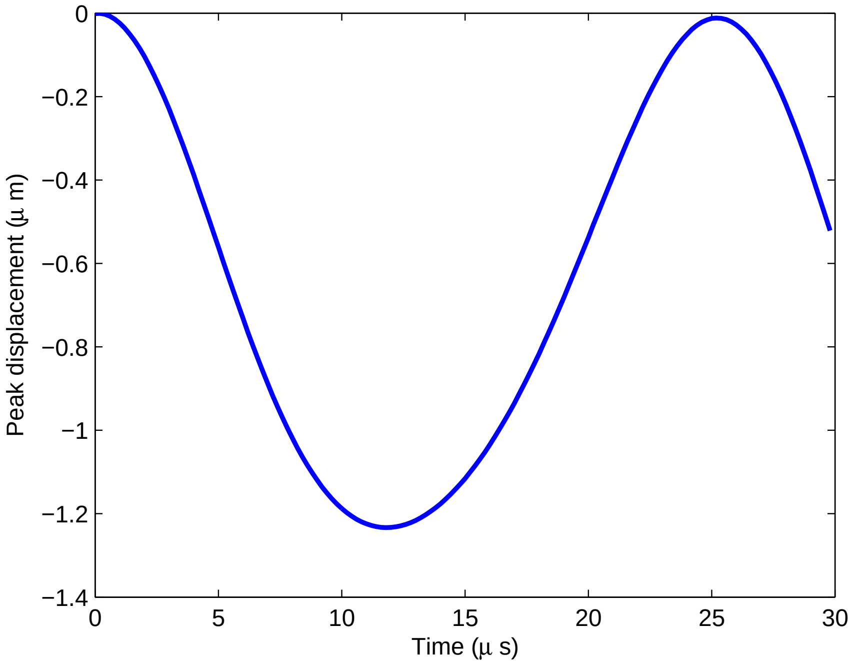

Figure 4.8: Dynamic response of Mirror C for a 20 V applied voltage.

position becomes longer until the voltage reaches a critical point where the increase of the electrostatic force becomes faster than the increase of the mechanical restoring force and the inertial force. The beam will be pulled down to the substrate beyond this critical pull-in voltage, as shown in Figure 4.2. The dynamic pull-in voltage of Mirror C is found to be 21.76 V.

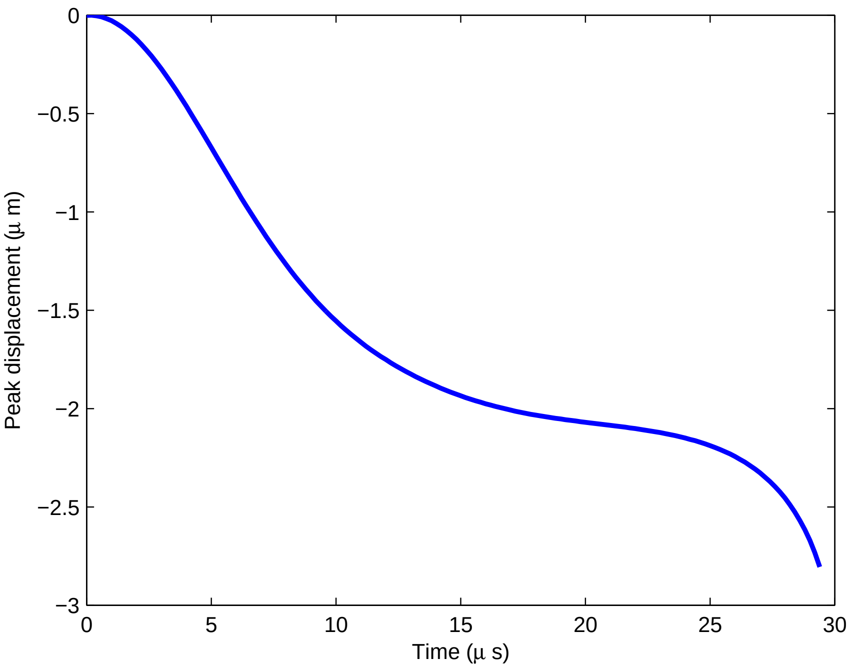

Figure 4.9: Dynamic pull-in of Mirror C.

Chapter 5

Input-Shaping Control of Microelectromechanical Mirrors

5.1 Open-Loop Control of Micromirrors

With the advances of microfabrication technology, high precision and reliable fabrication techniques become available for producing high quality MEMS devices. There is a pressing need for techniques that can be used to improve the dynamic behavior of MEMS, i.e., the response, speed, and precision. As introduced in Chapter 1, the performance of electrostatically actuated microelectromechanical mirrors can be improved by introducing control mechanisms in the operation of MEMS. For MEMS applications, input-shaping open-loop control is favorable due to its simplicity.

Typically, an electrostatically actuated micromirror is a single input (voltage) single output (rotation angle) system. In this case, open-loop control is even more attractive as the voltage input is relatively easy to manipulate. As discussed in Chapter 1, input-shaping control is an open-loop control approach in which a sequence of input impulses are applied in order to generate the desired results, as shown in Figure 5.1 [10]. The rotation of the mirror plate is a function of the applied voltage. For a constant input voltage V_1 the mirror plate oscillates about it's equilibrium position until the plate settles at the equilibrium position due to damping. The idea of the input-shaping is to introduce a second impulse voltage at the point where the mirror plate reaches its peak rotation angle. At that point, the rotational velocity of the mirror plate is zero. The magnitude of the second voltage impulse is chosen such that the static equilibrium rotation angle produced by V_1 is exactly the dynamic peak rotation angle shown in the figure. By using this approach, the residual vibration of the system is expected to be zero after the application of V_2. While the input-shaping control is attractive due to its simplicity, the effectiveness of this control scheme depends on the accuracy of the model that is used to compute the impulse voltages V_1 and V_2. Therefore, accurate modeling of the micromirror system is critical in the input-shaping process. Furthermore, the nonlinear electrostatic force imposes additional difficulties in the modeling. As discussed in Chapter 1, various approaches has been developed for input-shaping of lin-

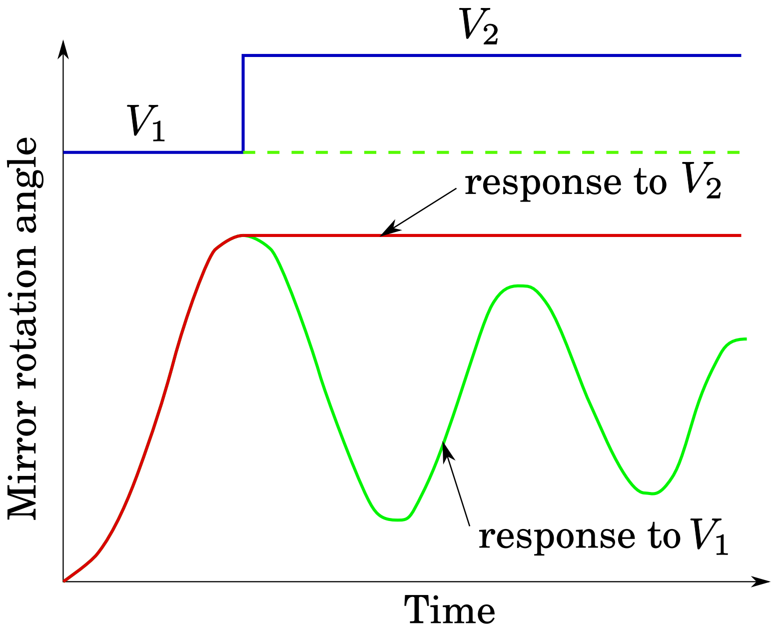

Figure 5.1: Schematic of input shaping.

ear systems. For the nonlinear micromirror system, an input-shaping control algorithm has also been proposed [10]. It has been shown that step-shaped input voltages can be used to control the structural vibration of MEMS. The input-shaping algorithm is based on an first order analytical lumped model. As the micromirrors have complex geometries and nonlinear behaviour, it is not clear to what extend these models are accurate. In addition, it is not clear what the effects of the higher vibrational modes are on the input-shaping control of MEMS and if it is possible to improve the input-shaping technique to control these effects. In this work, we investigate these input-shaping issues by using the full numerical model and the FEM/BEM solver we have developed.

5.2 Bending Mode Effect on Input Shaping

To investigate the bending mode effect, we first apply the step-shaped input voltage that can be obtained from the analytical model described in [10] for the three micromirrors shown in Chapter 1. In addition, with our coupled solver, we are able to compute the step-shaped input voltage from the numerical simulations: first we do a set of dynamic simulations to find the first voltage impulse voltage V_1 that produces desired peak deformation dynamically and record the time at which the mirror reaches the desired position. Next, we perform a set of static analysis to find the second impulse V_2 that produces desired deformation statically. Figure 5.2 compares the three mirrors we used. Mirror A and Mirror B have the same dimensions. However, the electrodes of Mirror B are closer to the center of the mirror plate. In Mirror C, the electrodes are placed close to the center of the mirror plate, the suspension beams are longer than those of Mirror A and B.

Figure 5.3 shows the step voltage and the dynamic response of Mirror A. The response matches the designed behavior quite well. However, the step-shaped voltage does not produce the desired dynamic behavior for Mirror B. There is still oscillation after the second impulse voltage as shown in Figure 5.4. Figure 5.5 shows the response of Mirror C. The residual vibration is very large in this case.

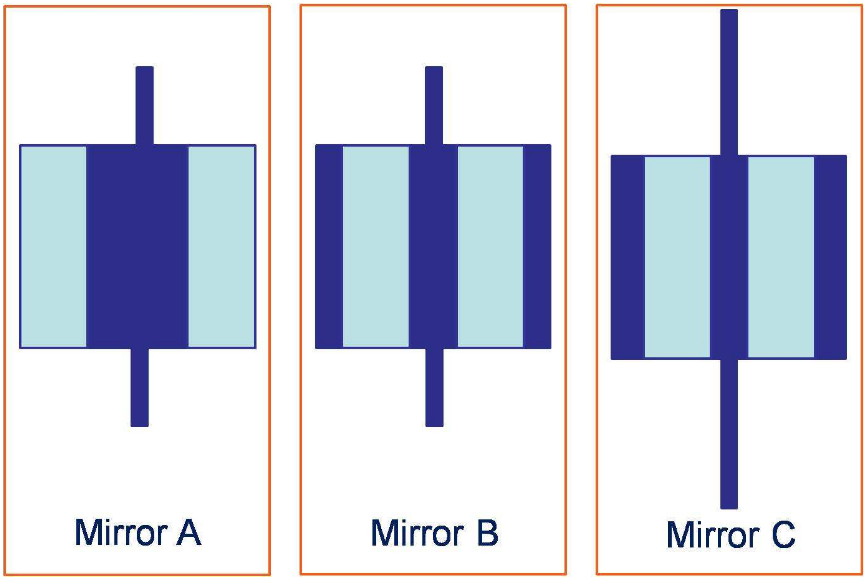

Figure 5.2: Dimension comparison of the mirrors.

Since the electrostatic force is always pointing downward, for a given electrostatic force, the ratio of the bending deformation to the torsional deformation depends on the ratio of the bending stiffness and the torsional stiffness of the beam. In addition, the bending/-torsional deformation ratio depends on the ratio of the total downward force and the torque exerted on the mirror. The bending stiffness of the beams can be determined by

$$k_{bending} = \frac{24EI_y}{l^3} \tag{5.1}$$

where E is the Young's modulus, $I_y = wh^3/12$ is the moment of inertia of the suspension beam cross section about the y-axis, and l is the length of the beam. The effective torsional stiffness of the beam is given by

$$k_{torsion} = \frac{2GJ}{l} \tag{5.2}$$

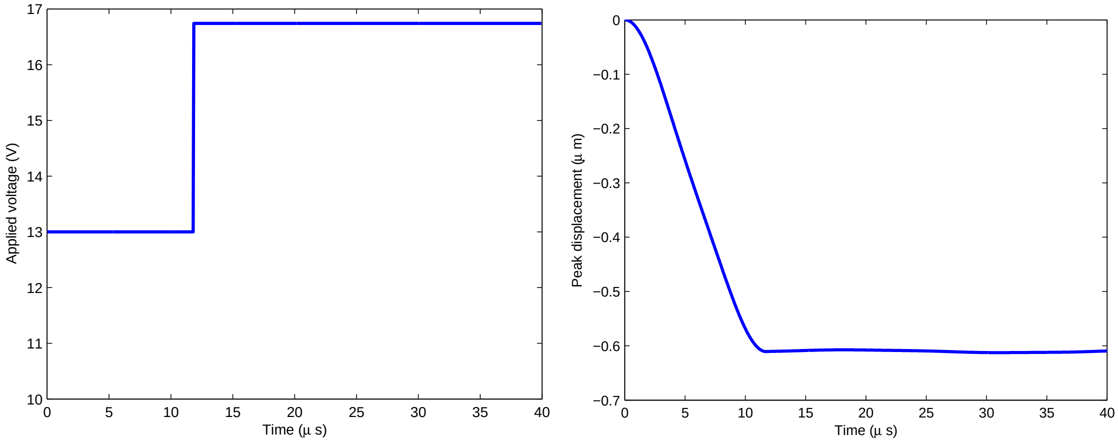

Figure 5.3: Step-shaped input voltage control: Mirror A.

where G is shear modulus that can be obtained as $G = E/(2+2\nu)$ and J is the polar moment of inertia of the beam cross section expressed as

$$J = \begin{cases} hw^3\left[\frac{1}{3} - 0.21\frac{w}{h}\left(1 - \frac{w^4}{12h^4}\right)\right] & for\ w \le t \\ hw^3\left[\frac{1}{3} - 0.21\frac{h}{w}\left(1 - \frac{h^4}{12w^4}\right)\right] & for\ w \ge t \end{cases} \tag{5.3}$$

The bending stiffness and torsional stiffness of the three mirrors calculated from the above equations are summarized in Table 5.1. It is shown that Mirror A and B have a larger bending/torsional stiffness ratio than Mirror C. For this reason, the bending mode effect is larger in Mirror C. Although Mirror A and Mirror B have the same bending/torsional stiffness ratio, the position of the electrodes of Mirror A is more towards the edge of the mirror plate, which results in a larger torque in Mirror A. The torque/pulling force ratio

Table 5.1: Bending stiffness and torsional stiffness of the torsional micromirrors.

	Mirror A	Mirror B	Mirror C
Bending Stiffness (N/m)	19.52	19.52	8.36
Torsional Stiffness (Nm)	2.22e-9	2.22e-9	2.47e-9

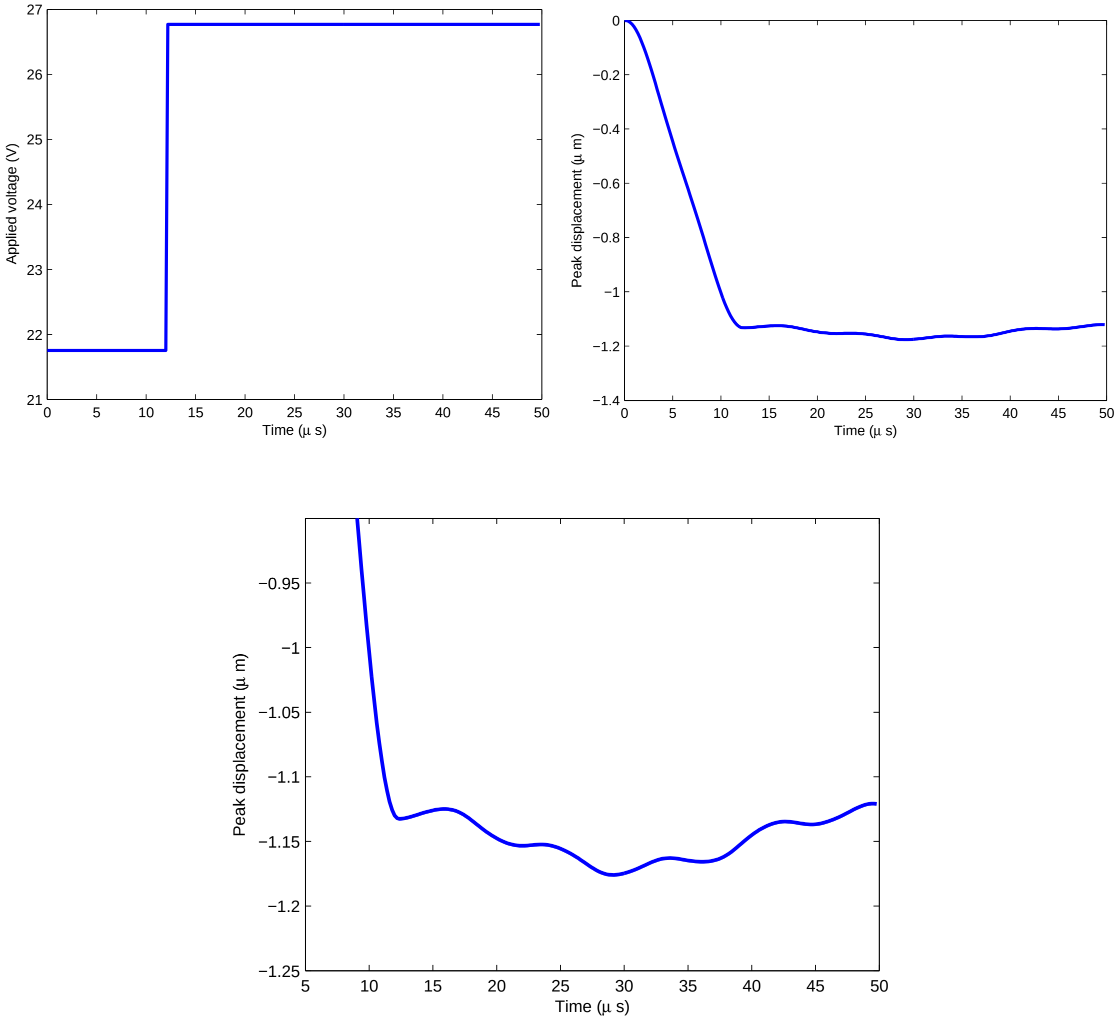

Figure 5.4: Step-shaped input voltage control: Mirror B.

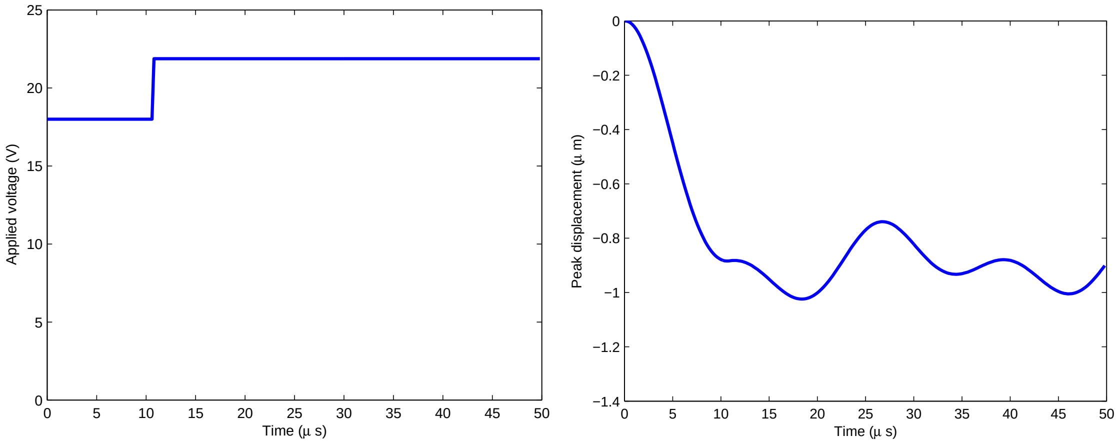

Figure 5.5: Step-shaped input voltage control: Mirror C.

is larger in Mirror A. The bending mode is barely excited in Mirror A and the resultant residual bending vibration in Mirror A is minimal. The step input voltage is sufficient in controlling the dominant torsional mode. However, for Mirror B, due to the position of the electrodes, more electrostatic energy is distributed to bend the beam, the bending mode appears after the torsional mode is suppressed by the step actuation voltage. In Mirror C, the bending deformation is even larger due to the low bending stiffness of the beam. Thus, both the bending/torsional stiffness ratio and the torque/pulling force ratio are important in determining the effect of the bending mode in the input-shaping of micromirrors.

5.3 Computational Input Shaping Optimization

It is clear that for mirror designs that have a low bending/torsional stiffness ratio and/or low the torque/pulling force ratio, the residual vibration due to the bending mode is large with the step-shaped input voltage. In this work, we propose to suppress the residual vibration by using an optimization technique in our numerical simulations. In order to find the correct shape of the input voltage, we seek to minimize the acceleration according to the real time dynamic response of the mirror. In this optimization problem, the objective function is simply the acceleration of a point on the edge of the mirror. The voltage is the single input to the system. The following system of equations are involved in the optimization process.

First, the Boundary Element Method is used to determine the electric field produced by the input voltage.

$$\mathbf{G}\mathbf{q}(\mathbf{d}_{n+1}) = \mathbf{u} \tag{5.4}$$

The surface charge density can be determined from the electric field by

$$\sigma = -\epsilon q \tag{5.5}$$

The surface pressure is related to the surface pressure exerted by the electrostatic force by

$$P \quad = \quad \frac{\sigma^2}{2\epsilon} \tag{5.6}$$

This Newmark Method is then used to calculate the acceleration of the next time step based on the surface pressure.

$$\begin{aligned}&\left(\mathbf{M} + \gamma\mathbf{C}\Delta t + \beta\Delta t^2\mathbf{K}\right)\ddot{\mathbf{d}}_{n+1} = \\ &\mathbf{P}_{n+1} - (\mathbf{C} + \Delta t\mathbf{K})\,\dot{\mathbf{d}}_n - \left(\Delta t(1-\gamma)\mathbf{C} + \frac{\Delta t^2}{2}(1-2\beta)\mathbf{K}\right)\ddot{\mathbf{d}}_n - \mathbf{K}\mathbf{d}_n\end{aligned} \tag{5.7}$$

The displacement at t_{n+1} can then be obtained

$$\mathbf{d}_{n+1} = \mathbf{d}_n + \Delta t\dot{\mathbf{d}}_n + \frac{\Delta t^2}{2}(1-2\beta)\ddot{\mathbf{d}}_n + \frac{\Delta t^2}{2}(2\beta)\ddot{\mathbf{d}}_{n+1} \tag{5.8}$$

The equations above are coupled nonlinear equations. A few methods are available to find an input voltage $\mathbf{u}$ that minimizes the acceleration $\ddot{\mathbf{d}}_{n+1}$. For example, the Newton method and the secant method. In this thesis, for the sake of simplicity, we employ a straightforward Bisection Method.

The Bisection Method is an optimization approach used to mostly to find the kernel of a function (i.e. $f(x) = 0$). For our case the acceleration is a function of the input voltage. If the input voltage for the mirror is chosen too low the mirror will deflect away from the electrode. If the input voltage for the mirror is chosen too high the mirror will deflect toward the electrode. To start the Bisection Method two initial voltages need to be chosen such that one voltage is too low and the other is too high for the intended purpose of minimizing the acceleration for the next time step these voltages are referred to as V_a and $V_b$respectively, as shown in Figure 5.6. A new voltage is chosen at the average of V_a and V_b and is called V_c. This bisects the distance between the voltages. The solution is in one of the two regions. V_c is relabelled the new V_a or V_b depending on which region the solution is in. This effectively cuts the distance between the previous V_a and V_b in half. Each iteration of the bisection method will narrow the range between V_a and V_b by half. The optimization

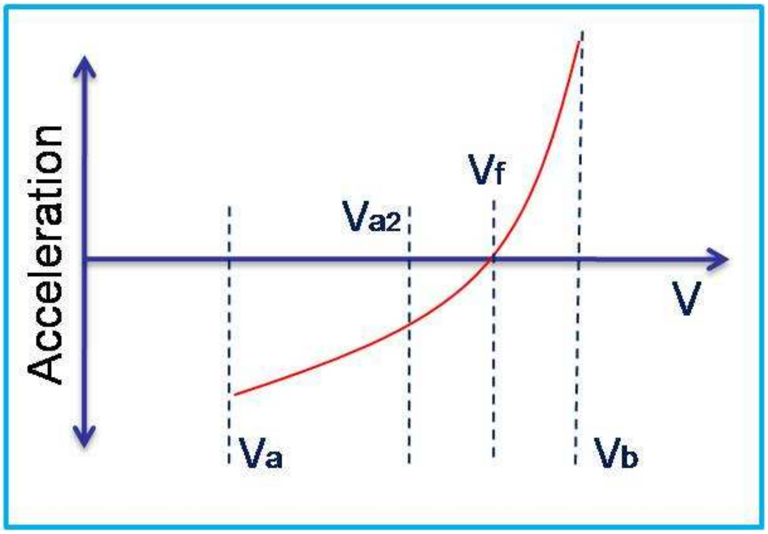

Figure 5.6: The Bisection Method

process is listed in Algorithm 4.

Algorithm 4 Input Shaping Optimization

```
1: Pick trial voltage as determined by the Bisection Method
2: Use BEM to determine the electric field based on the input voltage
3: Calculate the surface charge density from the electric field
4: Calculate the electrostatic pressure from the surface charge density
5: Calculate acceleration using the Newmark Method
6: Repeat until acceleration converges
```

Figures 5.7-5.9 show the optimized shape of input voltage for the three mirrors. For Mirror A, the optimized shape is almost identical to the step-shaped input voltage. Therefore, the optimization automatically reproduces the step-shaped input voltage if the residual vibration is small. The optimization procedure results in a periodic nonlinear input voltage design for both Mirror B and Mirror C. We observed that the frequency of the input voltage is close to the natural frequency of the bending mode, this suggests that this variation of the input voltage is used for compensating the bending vibration of the mirror. It is shown that the bending mode effect is effectively suppressed by the optimized shape of input voltage.

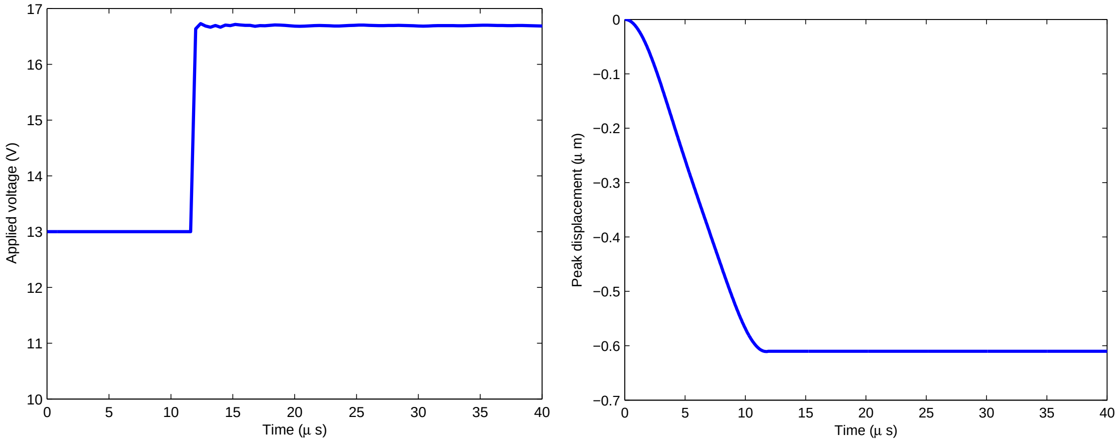

Figure 5.7: Optimized shape of input voltage: Mirror A.

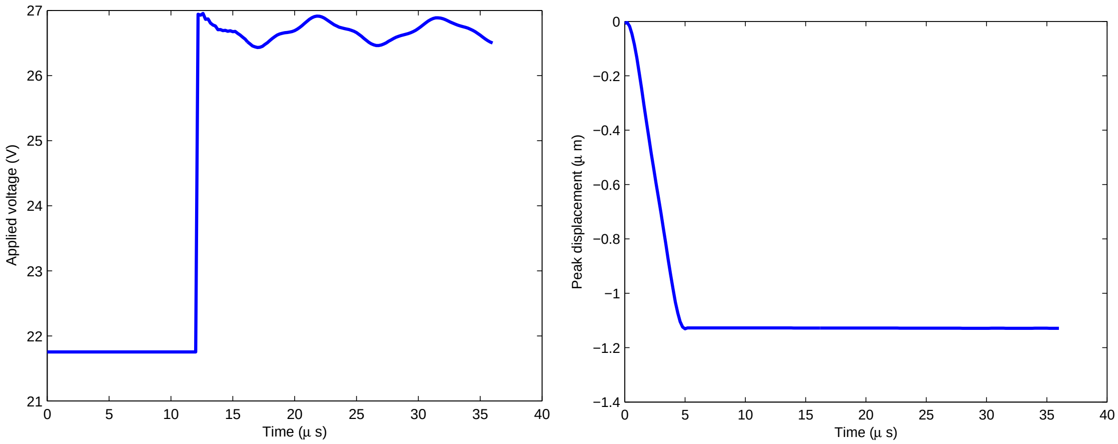

Figure 5.8: Optimized shape of input voltage: Mirror B

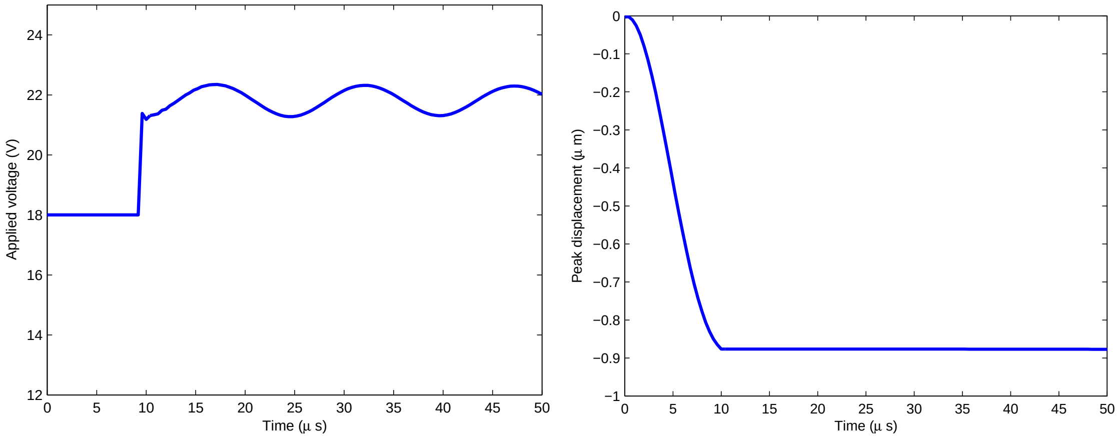

Figure 5.9: Optimized shape of input voltage: Mirror C

Chapter 6

Conclusion

In this work, we have developed a full 3-D MEMS simulation code for input-shaping open-loop control of electrostatic micromirrors. we show that the higher modes may have a significant effect on the residual vibrations of the system depending on the system parameters. The significance of the bending mode depends on the bending/torsional stiffness ratio and the torque/pulling force ratio. We employ a numerical optimization procedure to shape the input voltage from the real time dynamic response of the mirror structures. The optimization procedure results in a periodic nonlinear input voltage design that can effectively suppress the bending mode effect. Our results suggest that the periodic variation of the input voltage is for compensating the bending vibration of the mirror.

References

1. J.W. Judy, “Microelectromechanical systems (MEMS): Fabrication, design, and applications”, *Smart Materials and Structures*, vol 10, pp. 1115-1134, 2001.
2. H. Fujita, “A Decade of MEMS and its Future” in Proc. *10th IEEE Workshop Micro Electromech Syst.*, Nagoya Japan, pp. 1-8, 1997.
3. G. T. A. Kovas, *Micromachined Transducers Sourcebook*, McGraw-Hill, 1998.
4. G. Fedder, “Structure Design of Integrated MEMS,” Proc. of 12th IEEE Intl. Conf. on Micro Electro Mechanical Systems (MEMS ’99), Orlando, FL, pp. 1-8, 1999.
5. J. Wen, X. D. Hoa and A. G. Kirk, “Analysis of the Performance of a MEMS Micromirror,” *IEEE Transations on Magnetics*, vol. 40, no. 2, pp. 1410-1413, 2004.
6. V. Viereck, Q. Li, J. Achermann, A. Schwank, S.Araujo, A. Jakel, S. Werner, N. Dharmarasu, J. Schmid, and H. Hillmer, “Novel Large Area Applications Using Optical MEMS”*Optical MEMS and Nanophotonics*, IEEE/LEOS Internationl, pp 55-56, 2007.
7. D. Dudley, W. Duncan, J. Slaughter, “Emerging Digital Micromirror Device (DMD) Applications”, Proc SPIE, vol. 4985, pp. 14-25, 2003.
8. Nielson, G.N., Olsson, R.H., Resnick, P.R., Spahn, O.B.,””High-Speed MEMS Micromirror Switching, Lasers and Electro-Optics, 2007. CLEO 2007. Conference on , vol., no., pp.1-2, 6-11 May 2007.
9. B. Borovic, A.Q. Liu, D. Popa, H. Cai, F.L. Lewis, “Open-loop versus closed-loop control of MEMS devices: choices and issues”, *Journal of Micromechanics and Microengineering*, vol. 15, no. 10, pp. 19171924, Oct. 2005.
10. M. F. Daqaq, K. C. Reddy, and A. H. Nayfeh, Input-Shaping Control of Nonlinear MEMS, *Nonlinear Dynamics*, vol. 54, no. 1-2, 2008.
11. N. Singer, W. Seering, “Preshaping Command Inputs to Reduce System Vibrations”, ASME *Journal of Dynamic Systems Measurement and Control*, **112**(March): p76-82,1990.
12. Singhose, W.E.; Seering, W.P.; Singer, N.C., ”Shaping inputs to reduce vibration: a vector diagram approach,” Robotics and Automation, 1990. Proceedings., 1990 IEEE International Conference on , vol., no., pp.922-927 vol.2, 13-18 May 1990.

13. William Singhose, Lisa Porter, Michael Kenison, Eric Kriikku," Effects of hoisting on the input shaping control of gantry cranes", *Control Engineering Practice*, Volume 8, Issue 10, Pages 1159-1165, October 2000.

14. B. Borovic, C. Hong, A.Q. Liu, L. Xie, F.L. Lewis, "Control of a MEMS Optical Switch", 43rd IEEE Conference on Decision and Control, 2005.

15. Popa, D.O.; Byoung Hun Kang; Wen, J.T.; Stephanou, H.E.; Skidmore, G.; Geisberger, A., "Dynamic modeling and input shaping of thermal bimorph MEMS actuators," *Robotics and Automation*, 2003. Proceedings. ICRA '03. IEEE International Conference on , vol.1, no., pp. 1470-1475 vol.1, 14-19 Sept. 2003.

16. T. Yang, K. Chen, C. Lee, J. Yin, "Suppression of motion-induced residual vibration of a cantilever beam by input shaping", *Journal of Engineering Mathematics*, Volume 54, Number 1, pp1-15, 2006.

17. S. Mahmoodi, N. Jalili, "Non-linear vibrations and frequency response analysis of piezoelectrically driven microcantilevers", *International Journal of Non-Linear Mechanics*, vol. 42, Issue 4, pp 577-587, 2007.

18. T. Mukherjee, "Emerging Simulation Approaches for Micromachined Devices,"*IEEE Trans. Computer-Aided Design,* vol. 19, pp 1572-1589, Dec. 2000.

19. M. Schlegel, "Analyzing and Simulation of MEMS in VHDL-AMS Based on Reduced-Order FE Models", *Sensors Journal, IEEE,* vol.5, pp. 1019-1026 2005.

20. G. Li, "Efficient Mixed-Domain Analysis of Electrostatic Microelectromechanical System (MEMS)", PhD Dissertation, 2003.

21. G. Li, N.R. Aluru, "Efficient Mixed-Domain Analysis of Electrostatic MEMS", *IEEE Trans. Comput.-Aided Design.* vol. 22, pp.1228-1242, 2003.

22. R. D. Cook, D. S. Malkus, M. E. Plesha and R. J. Witt, *Concepts and Applications of Finite Element Analysis*, J. Wiley & Sons, 2001.

23. S.S. Rao, *The Finite Element Method in Engineering* 4th Ed., Elsevier Butterworth-Heinemann, 2005.

24. T.J.R. Hughes, *The Finite Element Method - Linear Static and Dynamic Finite Element Analysis*, Dover , 2000.

25. S.S. Rao, *Vibration of Continuous Systems*, John Wiley and Sons, 2007.

26. L.C. Wrobel, *The Boundary Element Method Vol.1 Applications in Thermo-Fluids and Acoustics*, John Wiley and Sons, 2002.

27. J. H. Kane, Boundary Element Analysis in Engineering Continuum Mechanics. Englewood Cliffs, NJ: Prentice-Hall, 1994.

28. F. Shi, P. Ramesh, and S. Mukherjee, "On the application of 2D potential theory to electrostatic simulation," *Communications in Numerical Methods in Engineering*, vol. 11, pp. 691701, 1995.

29. J.G. Korvink, O. Paul, *MEMS a practical guide to design, analysis and applications*, Willian Andrew Inc., Springer, 2006.

30. M.H. Aliabadi, W.S.Hall, “The regularising transformation integration method for boundary element kernels. Comparison with series expansion and weighted Gaussian integration methods”, *Engineering Analysis with Boundary Elements*, vol. 6, pp. 66-71, 1989.

31. M.H. Aliabadi, W.S.Hall, “Taylor Expansions for Singular Kernels in the Boundary Element Method”, *International Journal for Numerical Methods in Engineering*, vol. 21, pp.2221-2236, 1985.

32. G. Li, N.R. Aluru, “ Hybrid techniques for electrostatic analysis of nanoelectromechanical systems”, *Journal of Applied Physics*, vol. 96, number 4, pp. 2221-2231, 2004.

33. Z. Tang, Y. Xu, G. Li, N.R. Aluru, “Physical models for coupled electromechanical analysis of silicon nanoelectromechanical systems”, *Journal of Applie Physics*, vol. 97, 114304, 2005.

34. G. Li, N.R. Aluru, “Linear, nonlinear and mixed-regime analysis of electrostatic MEMS” *Sensors and Actuators*, vol. 91, pp. 278-291, 2001.

35. C. R. Vogel, Q. Yang, “Modeling, simulation, and open-loop control of a continuous facesheet MEMS deformable mirror”, *J. Opt. Soc. Am*, vol 23, number 5, pp.1074-1081, 2006.

36. G. Li, “New approximation and collocation schemes in the finite cloud method”, *Computers & Structures*, vol. 83, Issues 17-18, pp. 1366-1385, 2005.

37. J. Clark, “3D MEMS Simulation Modeling Using Modified Nodal Analysis”, Proc of the Microscale Systems: Mechanics and Measurements Symposium, pp. 68-75, 2000.

38. V. Litovski, “Behavioural Modelling, Simulation, Test and Diagnosis of MEMS using ANNs” in *Proceedings ISCAS*, 2005 .

Appendix

Code Construction

In order to model the electrostatically driven micro mirror. A coupled FEA/BEM solver was employed. The mesh for the FEA model was formulated using Abaqus. The surface nodes from the FEA were then used for the BEM mesh. Once the BEM mesh for the mirror is found the electrode will be meshed using a simple uniform meshing formula. The electrostatic pressure will now be found by use of the BEM. Once the surface pressure is known for the surface of the mirror, the force can be applied to the mirror. The natural and essential boundary conditions are now known for the mirror. The penalty method is used to enforce the essential boundary conditions. The displacement of the mirror due to the for applied by the electrode will be found by use of the FEA solver. For each time step the electrostatic pressure will change according to the position of the mirror, thus the BEM solver much be used for every time step. The Newmark method is utilized to solve for the displacement, velocity, and acceleration for each time step.

Figure 6.1 shows the process used for the dynamic electromechanical solver. Abaqus is used to mesh the domain. The nodes and element files are exported from Abaqus to a text file.The format for the nodes file, nodes.dat, can be seen in Table 6.1 The format for the elements file can be seen in Table 6.2 The element and node text files are then read into Surf. Surf determines the domain and creates the boundary conditions for the BEM solver, Table 6.3 and writes the BEM cells, Table 6.4 , and nodes,Table 6.5, to a text file based on the FEA mesh and a few boundary condition inputs. Surf also makes a key,Table 6.6, that relates the FEA nodes to the BEM nodes. The BEM solver reads the text files that where

Table 6.1: File format of nodes.dat

Node #	x - coord	y - coord	z - coord
1	1.0	2.0	0.0
⋮	⋮	⋮	⋮

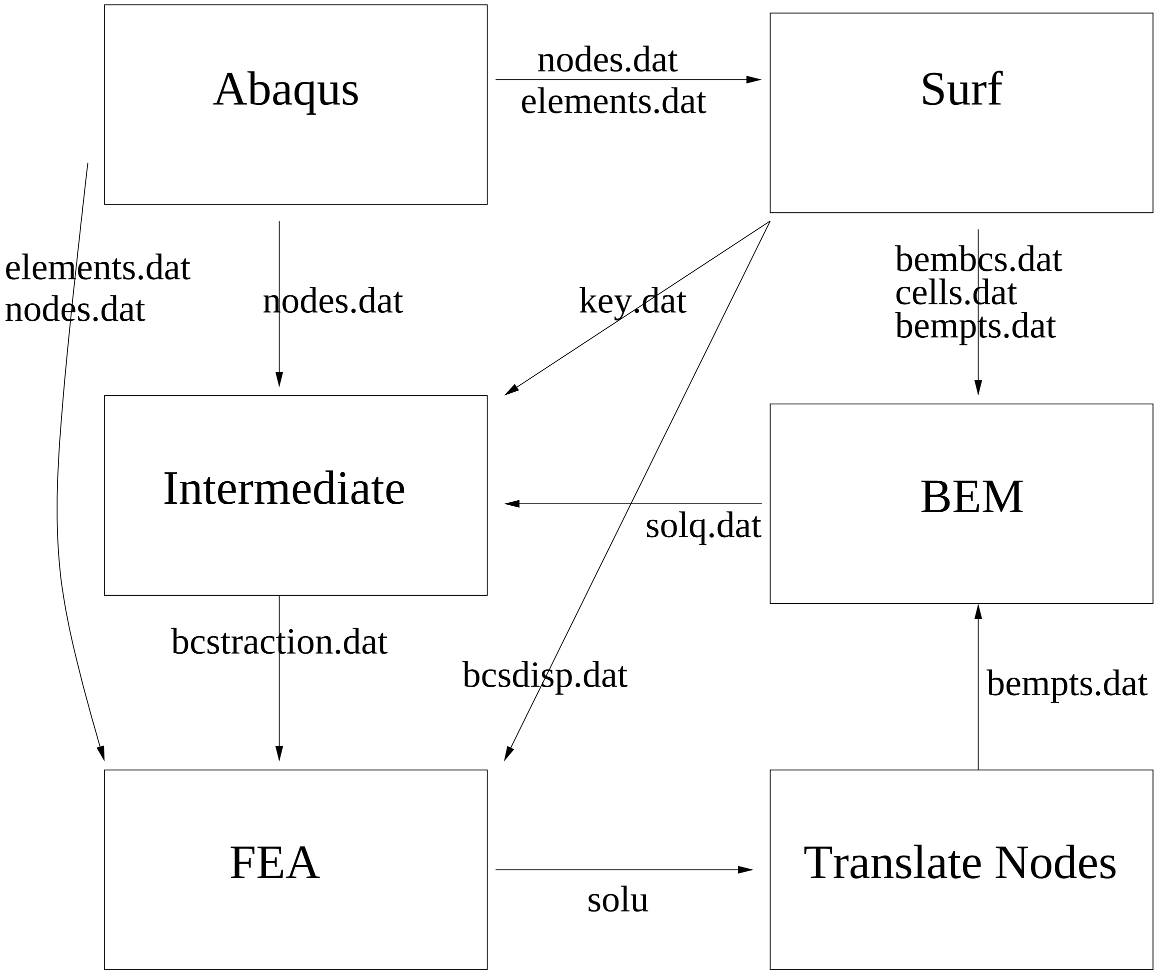

Figure 6.1: Class management flow chart.

Table 6.2: File format of elements.dat

Element #	node 1	node 2	node 3	node 4	node 5	node 6	node 7	node 8
1	603	394	46	47	1244	1035	687	688
⋮	⋮	⋮	⋮	⋮	⋮	⋮	⋮	⋮

Table 6.3: File format of bembcs.dat

node #	BC Type	BC Value
1	1	10
⋮	⋮	⋮

Table 6.4: File format of cells.dat

	node 1	node 2	node 3	node 4
Cell #	333	39	38	126
⋮	⋮	⋮	⋮	⋮

Table 6.5: File format of bempts.dat

Node #	x - coord	y - coord	z - coord
1	1.0	2.0	0.0
⋮	⋮	⋮	⋮

Table 6.6: File format of key.dat

FEA Element #	Face #	Node 1	Node 2	Node 3	Node 4
1	5	603	47	46	394
⋮	⋮	⋮	⋮	⋮	⋮

output by Surf and computes the surface pressures exerted by electrostatic forces. Intermediate reads in the forces from the BEM solver, the key from Surf, and the nodes from Abaqus to make the natural boundary conditions for the FEA solver, Table 6.7 . The FEA reads in the nodes and elements from Abaqus, the essential boundary conditions from Surf, Table 6.8 , and the natural boundary conditions from Intermediate. The FEA solver then determines the displacement of the nodes based on the forces as determined by the BEM solver. The nodal displacements are then read into Translate there is no file for the nodal displacements, they are input directly into the Translate function. Translate will update the BEM nodes to the deformed positions. The entire process will begin again for the next time step starting at the BEM solver. Note that Abaqus and Surf only have to run once. The process for the dynamic analysis can be seen in Figure 4.2.The ".dat" files that are listed are produced by the classes listed above them. Each file is available for any class below it on the flow chart and if a file is listed twice the one farthest down on the chart is the most recent.

Table 6.7: File format of bcs1.dat

Element #	Face #	Node 1	BC Value	0
0	0	Node 2	BC Value	0
0	0	Node 3	BC Value	0
0	0	Node 4	BC Value	0
⋮	⋮	⋮	⋮	⋮

Table 6.8: File format of bcs2.dat

	node #	Displacement	Rotation
x - direction	1	0	0
y - direction	1	0	0
z - direction	1	0	0
⋮	⋮	⋮	⋮